HHS Public Access

Author manuscript

Cell Rep. Author manuscript; available in PMC 2021 April 25.

Published in final edited form as:

Cell Rep. 2021 February 23; 34(8): 108773. doi:10.1016/j.celrep.2021.108773.

Neurexin1α differentially regulates synaptic efficacy within striatal circuits

M. Felicia Davatolhagh[1,2], **Marc V. Fuccillo**[2,3,*]

[1]Neuroscience Graduate Group, University of Pennsylvania, Philadelphia, PA 19104, USA

[2]Department of Neuroscience, Perelman School of Medicine, University of Pennsylvania, Philadelphia, PA 19104, USA

[3]Lead contact

SUMMARY

Mutations in genes essential for synaptic function, such as the presynaptic adhesion molecule Neurexin1α (Nrxn1α), are strongly implicated in neuropsychiatric pathophysiology. As the input nucleus of the basal ganglia, the striatum integrates diverse excitatory projections governing cognitive and motor control, and its impairment may represent a recurrent pathway to disease. Here, we test the functional relevance of Nrxn1α in striatal circuits by employing optogenetic-mediated afferent recruitment of dorsal prefrontal cortical (dPFC) and parafascicular thalamic connections onto dorsomedial striatal (DMS) spiny projection neurons (SPNs). For dPFC-DMS circuits, we find decreased synaptic strength specifically onto indirect pathway SPNs in both Nrxn1α$^{+/-}$ and Nrxn1α$^{-/-}$ mice, driven by reductions in neurotransmitter release. In contrast, thalamic excitatory inputs to DMS exhibit relatively normal excitatory synaptic strength despite changes in synaptic *N*-methyl-D-aspartate receptor (NMDAR) content. These findings suggest that dysregulation of Nrxn1α modulates striatal function in an input- and target-specific manner.

Graphical Abstract

*Correspondence: fuccillo@pennmedicine.upenn.edu.

AUTHOR CONTRIBUTIONS

Conceptualization, M.F.D. and M.V.F.; methodology, M.F.D. and M.V.F.; formal analysis, M.F.D.; investigation, M.F.D.; writing – original draft, M.F.D.; writing – review and editing, M.F.D. and M.V.F.; visualization, M.F.D. and M.V.F.; supervision, M.F.D. and M.V.F.; funding acquisition, M.V.F.

SUPPLEMENTAL INFORMATION

Supplemental information can be found online at https://doi.org/10.1016/j.celrep.2021.108773.

DECLARATION OF INTERESTS

M.V.F. is a member of the Cell Reports advisory board.

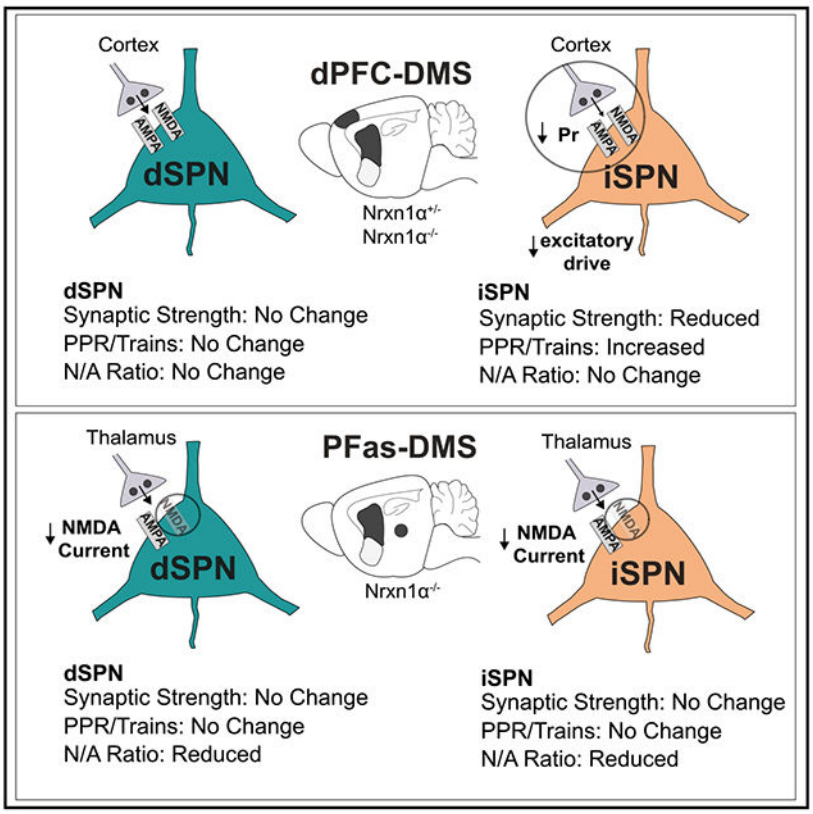

In brief

Davatolhagh and Fuccillo demonstrate that loss of Nrxn1α, a synaptic cell adhesion molecule, leads to divergent synaptic phenotypes within dorsal medial striatum for inputs from dorsal prefrontal cortex and parafascicular thalamic nucleus. These findings suggest input-specific imbalances in striatal circuit activity as a key perturbation in models of neurodevelopmental disorders.

INTRODUCTION

The striatum, as the input nucleus of the basal ganglia, integrates diverse neuronal projections governing cognitive and motor control (Balleine et al., 2009; Graybiel et al., 1994; Packard and Knowlton, 2002) and serves behavioral functions whose impairment is linked to neuropsychiatric disorders (Fuccillo, 2016; Yin and Knowlton, 2006). The principal striatal cell type, spiny projection neurons (SPNs), can be subdivided into two distinct neuronal populations: direct pathway SPNs (dSPNs), which target the substantia nigra pars reticulata (SNr) and express D1 dopamine receptors, and indirect pathway SPNs (iSPNs), which project to the globus pallidus and express D2 dopamine and adenosine A2A receptors (Gerfen et al., 1990). SPN activity is driven by excitatory inputs, receiving widespread forebrain glutamatergic projections from the cortex and thalamus (Ding et al., 2008; Pan et al., 2010). These excitatory projections have topographical organization (Deng et al., 2015; Gerfen, 1989; Hunnicutt et al., 2016), extensive molecular diversity, and distinct

synaptic properties (Ding et al., 2008; Smeal et al., 2008). This complexity has been a persistent obstacle in understanding how molecular dysfunction contributes to disease-relevant striatal circuit abnormalities.

As the number of neuropsychiatric disease-associated mutations grows, candidate genes have been parsed according to putative functions (Chang et al., 2015; Schizophrenia Working Group of the Psychiatric Genomics Consortium, 2014) and spatio-temporal cellular expression patterns (Willsey et al., 2013). Functionally, there is an overrepresentation of genes encoding DNA regulatory proteins, neuronal signaling regulators, and molecules essential for development and function of synapses, including synaptic adhesion proteins (Südhof, 2008, 2018; Willsey and State, 2015). Spatially, cortico-striato-thalamic (CST) circuits reliably exhibit enrichment in expression of candidate genes for both autism spectrum disorder (ASD) and schizophrenia (Chang et al., 2015; Skene et al., 2018; Willsey et al., 2013). Thus far, analysis of synaptic adhesion molecule function within CST circuits has centered on Neuroligin (NL) family postsynaptic proteins. Dorsal striatal recordings of NL1 knockout (KO) mice revealed a dSPN-specific reduction in the ratio of *N*-methyl-D-aspartate receptor (NMDAR) to α-amino-3-hydroxy-5-methyl-4-isoxazolepropionic acid receptor (AMPAR)-mediated currents, which likely contributed to increased grooming in these KOs (Blundell et al., 2010). In the nucleus accumbens, NL3 disruption selectively impaired synaptic inhibition of dSPNs, contributing to enhanced motor learning (Rothwell et al., 2014). Despite their extensive disease association and complex behavioral picture, the function of Neurexins (Nrxns), NL's presynaptic partners, within striatal circuits remains unexplored.

In mammals, Nrxns are encoded by three genes under control of alpha (α) and beta (β) promoters. Although they are key molecules mediating synapse organization and calcium-triggered neurotransmitter release (Missler et al., 2003), specific functions depend on Nrxn isoform, brain region, and synapse subtype. In hippocampal subiculum, Nrxn3 functions *trans*-synaptically to maintain postsynaptic AMPAR content, while β-Nrxns regulate release probability through modulation of endocannabinoid (eCB) signaling (Anderson et al., 2015). Within the Nrxn family, Nrxn1α exhibits a disproportional neuropsychiatric disease association, with numerous heterozygous loss-of-function alleles found in ASD, schizophrenia, Tourette syndrome, and obsessive-compulsive disorder (OCD) (Bucan et al., 2009; Castronovo et al., 2020; Ching et al., 2010; Dabell et al., 2013; Kim et al., 2008; Kirov et al., 2009; Lowther et al., 2017; Reichelt et al., 2012). Despite these findings, the physiological effects of Nrxn1α mutations have not been studied in striatum, and analysis of disease-relevant heterozygotes has not been explored in any brain region (Asede et al., 2020; Etherton et al., 2009).

Here, we assessed the functional integrity of striatal circuits in Nrxn1α$^{+/-}$ and Nrxn1α$^{-/-}$ mice using optogenetic tools to specifically interrogate excitatory afferents into striatum. Using a combined field/whole-cell recording configuration, we found a decrease in synaptic efficacy from dorsal prefrontal cortex (dPFC) inputs to dorsal medial striatum (DMS) specifically onto iSPNs. This reduction in excitatory strength resulted from a reduction in glutamate release that reduced dPFC-iSPN coupling across a broad range of naturalistic input frequencies. Furthermore, similar magnitude alterations were present in Nrxn1α

heterozygotes. In contrast, another key excitatory striatal circuit, parafascicular thalamic (PFas) inputs to DMS, exhibited normal overall synaptic strength but reduced synaptic NMDAR content onto both SPN subtypes and normal PFas-DMS coupling. Taken together, we identify input and target-specific alterations in striatal circuits of mice with both heterozygous and homozygous mutations in Nrxn1α.

RESULTS

Optogenetic-mediated afferent recruitment to examine synaptic strength

Neurexin1α heterozygote and homozygous KO mice were crossed onto the Drd1a-tdTomato bacterial artificial chromosome (BAC) transgenic line, permitting identification of dSPNs and putative iSPNs (Ade et al., 2011; Choi et al., 2019). Global assessment of striatal excitatory synaptic function through recording tetrodotoxin (TTX)-insensitive spontaneous miniature excitatory postsynaptic currents (mEPSCs) provided evidence of presynaptic alterations (Figures S1A and S1C) without accompanying changes in spine density onto either SPN subtype (Figures S1B and S1D). Because spontaneous inhibitory synaptic transmission appeared unaltered (Figures S2A and S2B), we focused our further investigation on glutamatergic striatal inputs. The complex integrative architecture of the striatum, wherein excitatory inputs from multiple forebrain and thalamic regions make widespread intermingled synapses with SPNs (Hunnicutt et al., 2016; Mandelbaum et al., 2019), together with evidence for distinct pathways of spontaneous and evoked synaptic release (Sara et al., 2005), complicates deeper interpretation of spontaneous excitatory transmission. In light of this and the non-selective nature of local electrical stimulation techniques for afferent fiber stimulation, we employed optogenetic-mediated recruitment to explore action potential-evoked excitatory transmission in specific striatal circuits.

Prior cell-type-specific monosynaptic tracing from spiny neuron and local interneuron subtypes within DMS revealed extensive connectivity from dPFC and PFas regions (Choi et al., 2019). To isolate dPFC-striatal circuits, we transduced dPFC with adeno-associated virus (AAV)-DJ-hSyn-ChIEF-2a-Venus and optically evoked synaptic release in the presence of gamma amino-butyric acid receptor (GABAR) blockade. We simultaneously performed striatal field/whole-cell recordings (maximum distance, 50 μm) (Choi et al., 2019; Xiong et al., 2015) using the fiber volley of the field to normalize for opsin-expressing fibers (Figure 1A). For each recorded neuron, the whole-cell EPSC amplitude was plotted against the field fiber volley across increasing light intensity (Figure S3), with the resulting regression coefficient used as a proxy of synaptic strength (Figure 1B; see STAR methods for details). This approach was sensitive over a range of release probabilities, as demonstrated by the dynamic changes in regression coefficient with alterations in release probability (Figures 1C and 1D).

Target-specific reductions in excitatory synaptic strength of dPFC-striatal circuits

Despite a robust increase in the frequency of mEPSCs on dSPNs, we noted no changes in EPSC versus fiber volley slope for dPFC-dSPN connections in either Nrxn1α heterozygote or KO mice as compared with wild-type (WT) littermate controls (WT: n = 17 cells, N = 7 animals, Het: n = 17 cells, N = 7 animals, KO: n = 17 cells, N = 9 animals; ANOVA, p =

0.2693) (Figures 1E and 1F). In contrast, we noted a significant ~50% reduction in the regression coefficient of both Nrxn1α heterozygote and KO mice onto iSPNs, suggesting a decrease in synaptic strength at this connection (WT: n = 14 cells, N = 3 animals, Het: n = 17 cells, N = 4 animals; KO: n = 13 cells, N = 3 animals; ANOVA, p = 0.0060, *post hoc* test Dunnett's test; WT versus Het: p = 0.0059, WT versus KO: p = 0.0166) (Figures 1G and 1H; Figure S4). Changes in AP-evoked synaptic strength can arise from mutation-associated alterations in presynaptic or postsynaptic function. Given neurexins presynaptic localization, we probed presynaptic release via paired-pulse ratio (PPR) analyses. Optical stimulation of dPFC fibers targeting striatum revealed no changes in the PPR onto dSPNs (WT: n = 24 cells, N = 4 animals; Het: n = 11 cells, N = 3 animals; KO: n = 27 cells, N = 4 animals; two-way ANOVA, interaction: p = 0.1215, inter-stimulus interval [ISI]: p < 0.0001, genotype: p = 0.2405), across genotypes (Figure 2A), again in contrast with the observed increase in mEPSC frequency of dSPNs. Consistent with these data, there were no changes in the five-pulse variable frequency trains onto dSPNs across the three frequencies measured, including 10, 20, and 50 Hz (WT: n = 18 cells, N = 4 animals; Het: n = 11 cells, N = 3 animals; KO: n = 24 cells, N = 4 animals; two-way ANOVA, 10 Hz, interaction: p = 0.5466, Pulse#: p < 0.0001, genotype: p = 0.2182; 20 Hz, interaction: p = 0.0655, Pulse#: p < 0.0001, genotype: p = 0.5997; 50 Hz, interaction: p = 0.0003, Pulse#: p < 0.0001, genotype: p = 0.2407) (Figure 2B). To determine that a floor effect from optogenetic-associated decreases in PPR are not occluding potential increases in release probability for dPFC-SPN connections, we minimized direct terminal illumination by localizing a 50 μm 470 nm light spot at the corticostriatal border. PPR was not significantly higher in spot compared with full-field illumination (Figures S5A-S5C). Nevertheless, we tested dPFC-dSPN short-term dynamics in WT and Nrxn1α KO mice with spot illumination and reduced extracellular Ca^{2+}, again detecting no genotypic differences (Figures S5D and S5E).

In contrast with the dPFC-dSPN pathway, we noted an increase in the PPR onto iSPNs (WT: n = 19 cells, N = 4 animals; Het: n = 14 cells, N = 3 animals; KO: n = 20 cells, N = 5 animals; two-way ANOVA, interaction: p = 0.1286, ISI: p < 0.0001, genotype: p = 0.0178) in both Nrxn1α heterozygote and KO mice (Figure 2D). Furthermore, there was an increase in the ratios of the nth pulse/first pulse of the five-pulse variable frequency trains onto iSPNs (WT: n = 18 cells, N = 5 animals; Het: n = 14 cells, N = 3 animals; KO: n = 18 cells, N = 5 animals; two-way ANOVA, 10 Hz, interaction: p = 0.5342, Pulse#: p < 0.0001, genotype: p = 0.0068; 20 Hz, interaction: p = 0.0200, Pulse#: p < 0.0001, genotype: p = 0.0054; 50 Hz, interaction: p = 0.2991, Pulse#: p < 0.0001, genotype: p = 0.0010) (Figure 2E). To probe postsynaptic function, we measured optical NMDA/AMPA ratios, observing no changes onto either cell type (dSPNs—WT: n = 21 cells, N = 4 animals, Het: n = 13 cells, N = 3 animals, KO: n = 26 cells N = 4 animals; iSPNs—WT: n = 22 cells, N = 5 animals, Het: n = 14 cells, N = 3 animals, KO: n = 26 cells, N = 6 animals; ANOVA, dSPN: p = 0.0968, iSPN: p = 0.2986) (Figures 2C and 2F; Figures S6A and S6B). These results suggest a target-selective decrease in excitatory synaptic strength at dPFC-iSPN synapses, driven by reductions in presynaptic transmitter release probability.

Neurexin1α deletion alters postsynaptic function at thalamostriatal synapses through a reduction in NMDAR current

Because Nrxn1α is expressed at roughly similar levels across striatal afferent sites (Fuccillo et al., 2015), we wanted to determine whether the above reported synaptic changes were a common property across striatal projecting regions or were specific to this cortical input. We therefore targeted another region that densely innervates DMS, examining synaptic properties from the parafascicular nucleus of thalamus (Choi et al., 2019; Ellender et al., 2013; Mandelbaum et al., 2019) (Figure 3A). Using identical simultaneous field/whole-cell recordings, we measured the input-output relationship onto both SPN subtypes. Surprisingly, linear regression analysis revealed no genotypic differences for PFas excitatory synaptic connections onto either SPN subtype (dSPN—WT: n = 16 cells, N = 9 animals, KO: n = 17 cells, N = 6 animals; iSPN—WT: n = 13 cells, N = 8 animals, KO: n = 13 cells, N = 7 animals; unpaired two-tailed t test, dSPN: p = 0.9405, iSPN: p = 0.2578) (Figures 3B-3E). Consistent with this result, no changes were observed in PPR (Figures 4A and 4D) (dSPN—WT: n = 23 cells, N = 7 animals, KO: n = 20 cells, N = 6 animals; two-way ANOVA, interaction: p = 0.2456, ISI: p < 0.0001, genotype: p = 0.5276; iSPN—WT: n = 20 cells, N = 7 animals, KO: n = 18 cells, N = 6 animals; two-way ANOVA, interaction: p = 0.7044, ISI: p < 0.0001, genotype: p = 0.3267) or five-pulse variable frequency trains (Figures 4B and 4E) (dSPN—WT: n = 23 cells, N = 7 animals, KO: n = 18 cells, N = 6 animals; two-way ANOVA, 10 Hz, interaction: p = 0.5950, Pulse#: p < 0.001, genotype: p = 0.6032; 20 Hz, interaction: p = 0.4499, Pulse#: p < 0.0001, genotype: p = 0.5090; 50 Hz, interaction: p = 0.1235, Pulse#: p < 0.0001, genotype: p = 0.1769; iSPN—WT: n = 17 cells, N = 7 animals; KO: n = 17 cells, N = 6 animals; two-way ANOVA, 10 Hz, interaction: p = 0.5961, Pulse#: p < 0.0001, genotype: p = 0.3026; 20 Hz, interaction: p = 0.1262, Pulse#: p < 0.0001, genotype: p = 0.1607; 50 Hz, interaction: p = 0.1146, Pulse#: p < 0.0001, genotype: 0.4485) onto either SPN subtype. To probe for postsynaptic alterations, we measured optical NMDA/AMPA ratios, detecting a significant decrease in the Nrxn1α KO mice onto both SPN subtypes (Figures 4C and 4F; ANOVA, dSPN: p = 0.0149, iSPN: p = 0.0056; *post hoc* test Dunnett's test dSPN WT versus KO: p = 0.0080, iSPN WT versus KO: p = 0.0029). Furthermore, we observed a significant decrease in NMDA decay at synapses onto iSPNs, suggesting alterations in subunit composition (Figures S6C and S6D). Furthermore, analysis of Nrxn1α heterozygotes revealed an intermediate reduction in N/A ratio on both SPN subtypes that did not reach statistical significance (Figures 4C and 4F; *post hoc* test Dunnett's test; dSPN WT versus Het: p = 0.1639, iSPN WT versus Het: p = 0.3180). These results suggest that, in contrast with a presynaptic phenotypic locus at dPFC synapses in striatum, removal of Nrxn1α alters postsynaptic function at PFas-DMS synapses onto both SPN subtypes, without impacting release probability.

Enhanced eCB signaling through the anandamide (AEA) pathway at dPFC-iSPN synapses

eCBs are lipid-derived molecules that act as retrograde signals to limit presynaptic release probability at corticostriatal synapses (Ade and Lovinger, 2007; Choi and Lovinger, 1997; Gerdeman et al., 2002; Huang et al., 2001). Previous work has implicated β-neurexins and NL3 in regulation of eCB signaling (Anderson et al., 2015; Földy et al., 2013), suggesting that reduced presynaptic corticostriatal transmission onto iSPNs in Nrxn1α mutants could result from an increase in eCB-mediated synaptic depression. eCB-long-term depression

(LTD) is reliably induced through application of the type I metabotropic glutamate receptor (mGluR) agonist (*S*)-3,5-dihydroxyphenylglycine (DHPG) with coincident SPN depolarization to induce calcium influx through L-type calcium channels (Kreitzer and Malenka, 2005). Bath application of DHPG (50 μM for 10 min) while depolarizing post-synaptic neurons to −55 mV revealed no differences (WT: n = 12 cells, N = 3 animals, KO: n = 19 cells, N = 5 animals; two-tailed Student's t test, PPR% p = 0.2504) between genotypes for DHPG-mediated amplitude or PPR changes (Figures 5A and 5B). Studies suggest that eCB release by activation of postsynaptic mGluRs is primarily mediated by the endogenous cannabinoid 2-arachidonoylglycerol (2-AG) (Maccarrone et al., 2008; Tanimura et al., 2010).

To explore whether enhanced AEA signaling could be mediating the reduction in corticostriatal synaptic transmission onto iSPNs in Nrxn1α mutants, we pharmacologically inhibited degradation of AEA via bath application of URB 597, a selective inhibitor of fatty acid amid hydrolase (FAAH). Although bath application of URB 597 led to a similar reduction in optically evoked excitatory transmission in both WT and KO animals, we found that the accompanying PPR increase in WT mice was occluded in slices from KO animals (Figures 5D and 5E; WT: n = 19 cells, N = 6 animals; KO: n = 22 cells, N = 7 animals; two-tailed Student's t test, p = 0.0343). Concerned that rundown associated with whole-cell dialysis (Chen et al., 2011) might occlude amplitude changes (Figure 5C), we measured the slope of optical fields, which recapitulates the reduced corticostriatal synaptic transmission seen in Nrxn1α KOs (Figure 5F; two-tailed Student's t test, p = 0.0495). The magnitude of reduction of slope in response to bath application of URB 597 was significantly lower in Nrxn1α KO as compared with WT, suggesting occlusion of the effects of reduced AEA degradation in KOs (Figure 5G; two-tailed Student's t test, p = 0.0387). Together, these findings suggest that the loss of Nrxn1α increases mobilization of AEA, leading to enhanced eCB-mediated depression at dPFC-iSPN synapses.

Reduced responsiveness to *in vivo*-modeled input frequencies at iSPN corticostriatal terminals

It remains unclear how these diverse Nrxn mutation-associated changes would influence information transfer in the context of more intact circuits. To examine this issue, we generated *in vivo*-modeled optical stimulus patterns by using *in vivo* single-unit recordings as a mask to filter Poisson distributed cortical spike trains of frequencies typical of dPFC and PFas regions (5, 15, and 25 Hz, details in STAR methods) (Figure 6A; Figure S7A). Experiments were performed in current-clamp, holding the neuron at −55 mV to mimic the *in vivo* "up-state" membrane potential (Stern et al., 1997, 1998), and GABAergic inhibition was left intact. Total spiking efficiency (action potentials/number of optical stimuli) in Nrxn1α mutants was unchanged relative to WT for dSPNs (Figure 6B; two-tailed Student's test, p = 0.4714) but decreased for iSPNs in both Nrxn1α heterozygote and homozygote mice (Figure 6D; two-tailed Student's test, p = 0.0230). Input-output coupling deficiencies were observed at dPFC-iSPN connections across all tested input frequency domains (Figures 6C and 6E; two-way ANOVA, dSPN, interaction: p = 0.8340, frequency: p < 0.0001, genotype: p = 0.4387; iSPN, interaction: p = 0.3764, frequency: p < 0.0001, genotype: p =

0.0181). These results were not the result of biases in initial EPSP amplitude and did not depend on recording duration (Figures S7B-S7I).

To explore whether Nrxn1α-associated reductions in NMDAR function at PFas-DMS synapses could similarly perturb spiking efficiency, we presented our optical stimulus patterns. Total spiking efficiency was unchanged in the Nrxn1α KOs onto dSPNs (Figure 7A; two-tailed Student's t test, $p = 0.1196$) and iSPNs (Figure 7C; two-tailed Student's t test, $p = 0.1567$), and spiking efficiency was similar between genotypes across frequency domains (Figures 7B and 7D; two-way ANOVA, dSPN, interaction: $p = 0.4630$, frequency: $p = 0.0168$, genotype: $p = 0.1199$; iSPN, interaction: $p = 0.8298$, frequency: $p = 0.0013$, genotype: $p = 0.1701$). Together these findings suggest that the target-cell-specific reductions in release probability observed for dPFC-iSPN circuits have selective impact on the fidelity of corticostriatal connectivity.

DISCUSSION

Neurexins are presynaptic cell-adhesion molecules exhibiting diverse synaptic functions dependent on cell type and neural circuit context (Etherton et al., 2009; Südhof, 2008, 2018). Here, we show that Nrxn1α differentially regulates glutamatergic excitatory synaptic transmission at dPFC and PFas inputs to DMS. In both Nrxn1α heterozygous and homozygous animals, we observed reductions in probability of release onto iSPNs, but not dSPNs, at dPFC inputs to DMS. In Nrxn1α KOs, this reduction is in part due to enhanced AEA signaling altering dPFC-iSPN synapses. We demonstrated that reduced synaptic efficacy onto iSPNs is not a common feature of all striatal targeting inputs, because PFas inputs have normal release probability, while exhibiting altered post-synaptic NMDAR function. These findings provide further evidence that synaptic transmission regulated by Nrxn1α is input and target specific, illustrating its role within striatal circuits.

Challenges of studying presynaptic Nrxn1α function in striatal circuits

Advances in understanding the role of cell-adhesion molecules located pre-synaptically have been hampered by technical challenges. Earlier studies employing electrical stimulation were limited by the heterogeneity of stimulated inputs, as well as the substantial recruitment of systems that modulate neuronal function (Cavaccini et al., 2018; Kreitzer and Malenka, 2007; Shen et al., 2008). To gain access to specific striatal circuits, we utilized optogenetics, permitting light-mediated selective recruitment of either dPFC or PFas striatal inputs through the expression of a channelrhodopsin variant, ChiEF-2a-Venus (Lin et al., 2009). To normalize for differences in viral expression, we employed a combined field and whole-cell recording approach (Choi et al., 2019). The optically evoked field recorded in striatum is composed of two negative components (N1, N2) (Kupferschmidt et al., 2017), with the first negativity being largely composed of presynaptic opsin-expressing fibers. We used this signal as a normalization measurement for afferent recruitment when measuring whole-cell currents onto neighboring neurons. This approach provides an important step forward for understanding long-range synaptic connectivity, circumventing limitations regarding efficacy of viral transduction (Chuhma et al., 2011; Lenz and Lobo, 2013; Miesenböck, 2011). Furthermore, it permits more targeted access to specific regions than that provided by

broadly expressed Cre recombinase (Cre) lines (Rbp4-Cre, Thy1-Cre) previously employed to measure synaptic strength. A limitation of this technique is the requirement for relatively dense targeting by the afferent population, which is necessary to observe a clear, reliable optical fiber volley.

Convergent physiological phenotypes in Nrxn1α$^{+/-}$ and Nrxn1α$^{-/-}$ mice

Genes encoding proteins that support the formation and maintenance of synapses are significantly associated with ASD and schizophrenia (Chang et al., 2015). Disease-associated mutations in *Nrxn1* are commonly found as heterozygous copy number variations (CNVs) (Autism Genome Project Consortium et al., 2007; Castronovo et al., 2020; Huang et al., 2017; Lowther et al., 2017; Marshall et al., 2017). Behavioral studies using mice with either heterozygous or homozygous Nrxn1α deletions reveal non-overlapping phenotypes, with KOs exhibiting elevated anxiety levels, increased aggressive behaviors, nest building impairments, and altered social behaviors not observed in heterozygotes (Grayton et al., 2013). Despite this phenotypic divergence, Nrxn1α homozygous deletions have been the central focus of physiological analyses in rodents (Etherton et al., 2009). Studies in human embryonic stem cells highlight the relevance of heterozygous deletions, revealing substantial impairments in excitatory synaptic transmission (Pak et al., 2015). It nevertheless remains unclear whether haplo insufficiency of Nrxn1α disrupts neuronal physiology in disease-relevant neural circuits. Our data clearly demonstrate synaptic impairments within dPFC-iSPN circuits of roughly similar magnitude in both Nrxn1α heterozygous and homozygous mice. These data contrast with the absence of excitatory synaptic phenotypes in cortical primary neuronal cultures from Nrxn1α heterozygous and homozygous mice (Pak et al., 2015), highlighting the diversity of Neurexin function dependent on synaptic context (Anderson et al., 2015; Aoto et al., 2013).

Nrxn1α regulates synaptic transmission at dPFC-DMS synapses in a cell-type-specific manner

An interesting aspect of our study is the specificity of altered dPFC glutamatergic transmission dependent on target SPN subtype. Mice with either heterozygous or homozygous deletion of Nrxn1α were observed to have decreased synaptic strength onto striatal iSPNs. Although generally consistent with reductions in input-output strength observed at CA1 hippocampal synapses (Etherton et al., 2009), here we note the reduction in synaptic strength onto striatal iSPNs likely results from decreased release probability, as demonstrated by elevated PPRs and reductions in synaptic depression upon high-frequency stimulation. One interesting aspect of this phenotype is that cortico-striatal afferents do not show significant target neuron specificity, as evidenced both by cell-type-specific retrograde rabies labeling (Wall et al., 2013) and single axonal tracing (Doig et al., 2010). Although this lack of anatomical specificity contrasts with our observed synaptic phenotypes, it is possible that the differential transcriptome profiles in dSPNs and iSPNs contributes to the exclusivity of the synaptic phenotypes observed in this study (Doyle et al., 2008; Heiman et al., 2008). Similarly, it may be that molecular diversity of Neurexin signaling exists at the individual spine level, an interesting hypothesis awaiting higher resolution transcriptomic and proteomic approaches.

Previous work demonstrated that presynaptic β-Neurexins inhibit tonic eCB synthesis, thereby maintaining hippocampal CA1-subicular synaptic strength (Anderson et al., 2015), while postsynaptic NL3 regulates tonic eCB signaling to constrain hippocampal basket cell inhibition (Földy et al., 2013). Given these data, we tested whether observed decreases in release probability and synaptic strength in dPFC-iSPN circuits of Nrxn1α mutants resulted from dysregulation of eCB-mediated control. Our data suggest that loss of Nrxn1α function leads to enhanced AEA signaling that may lower synaptic release at dPFC-iSPN connections. This hypothesis may also explain the observed input (dPFC, but not PFas) and target (iSPN, but not dSPN) specificity insofar as (1) higher CB1R expression patterns in cortex than thalamus restrict eCB-mediated depression to corticostriatal synapses (Wu et al., 2015) and (2) AEA may bias depression toward the iSPN subtype (Ade and Lovinger, 2007; Giuffrida et al., 1999).

Nrxn1α maintains NMDAR function at PFas-DMS synapses onto both DMS SPN subtypes

Given the broad expression of *Nrxn1* throughout striatal-targeting projections, we asked whether alterations in synaptic efficacy are unique to dPFC-striatal circuits. We employed similar optogenetic methods to probe PFas inputs to the dorsal striatum but did not detect changes in synaptic strength or release probability. Interestingly, in contrast with dPFC-DMS synapses, NMDA/AMPA ratios at PFas-DMS synapses were reduced onto both SPN subtypes in KO mice. Furthermore, heterozygotes showed an intermediate reduction in NMDA/AMPA ratio, suggesting gene haploinsufficiency for this synaptic phenotype. We hypothesize that this reduced ratio results from a decrease in NMDAR currents for several reasons: (1) increases in AMPAR current should have increased the input/output slope measurements, (2) there was no evidence for changes in the amplitude of excitatory mEPSCs (although PFas neurons represent only a fraction of the total inputs recorded with this technique), and (3) triple KO of α-neurexins was observed to reduce NMDAR function in cultured neocortical slices (Kattenstroth et al., 2004). Although reduced synaptic NMDAR content may reflect a decrease in postsynaptic recruitment of NL1, which is known to mediate clustering of NMDARs (Blundell et al., 2010; Budreck et al., 2013; Wu et al., 2019), the lack of this phenotype at dPFC-striatal synapses is puzzling. It is worth considering the disconnect between our original spontaneous transmission data and the complexity of the dPFC and PFas synaptic phenotypes observed with pathway-specific optical recruitment. Whether these discrepancies arise from the diverse nature of excitatory afferent projections into DMS or represent the parallel actions of spontaneous and action-potential-evoked synaptic transmission pathways is yet unclear (Kavalali, 2015).

Changes to striatal circuit output and its implications

Cortical and thalamic regions exhibit topographic projections to discrete striatal compartments, where their control of SPN activity and local inhibitory circuits is an initial step in the generation of motor output. We extended our initial discovery of reduced synaptic strength in dPFC-iSPNs circuits of Nrxn1α$^{-/-}$ mice by probing the fidelity of spike production for dPFC inputs modeled on *in vivo* activity patterns. Consistent with our target-cell-specific effects, we found that dPFC-iSPN, but not dPFC-dSPN circuits of Nrxn1α heterozygote and homozygote mutants exhibited reduced total spiking efficiency across a range of frequency domains. Given that the prolonged “up-state”-like depolarizations

employed here are more akin to the sustained plateau-like depolarizations seen in *in vivo* recordings from anesthetized animals (Stern et al., 1998; Wilson and Groves, 1981; Wilson and Kawaguchi, 1996), as opposed to those observed during wakefulness (Mahon et al., 2006; Sippy et al., 2015), multi-site *in vivo* recordings during behavior will be required to clearly understand the effects of these synaptic phenotypes in dynamic circuits. Nevertheless, this selective decrease in cortical-iSPN excitatory drive is expected to promote disinhibition of thalamic structures projecting back to the cortex. It is an interesting future question as to whether this thalamic disinhibition can explain both simple motor phenotypes (e.g., hyperactivity, aggression) (Etherton et al., 2009; Grayton et al., 2013) and more complex reward-processing deficits observed in mice with Nrxn1α mutations (Alabi et al., 2020). It is worth noting a recent study of the *Tsc1* deletion ASD mouse model, which exhibited increased corticostriatal connectivity selectively onto dSPNs, with synaptic strength unperturbed at thalamostriatal synapses (Benthall et al., 2018). Another ASD model, *Shank3* deletion, was also found to have a selective reduction in glutamatergic synaptic transmission onto iSPNs (Wang et al., 2017). Together with our data, this raises the possibility that disinhibition of basal ganglia-targeted thalamus is a common circuit disruption for ASD pathophysiology with clear implications for downstream cortical activity.

Here, we demonstrated that the loss of Nrxn1α has differential effects within striatal circuits, extending the literature suggesting imbalances in basal ganglia activity as a common perturbation in models of neurodevelopmental disorders (Benthall et al., 2018; Espinosa et al., 2015; Rothwell et al., 2014; Wang et al., 2017). Our data highlight the challenges that context-dependent gene function creates for understanding molecular contributions to brain and behavioral pathology. These distinctions are even apparent for cortical sub-regions, which display profound heterogeneity in anatomical and functional connectivity to striatum, as well as divergent synaptic phenotypes in response to loss of the postsynaptic scaffolding molecule SAPAP3 (Corbit et al., 2019). Given that genes related to synaptic function are implicated in neuropsychiatric disease, detailed circuit-specific studies *in vitro* and *in vivo* are needed to elucidate context-specific functions and better understand how synaptic dysregulation contributes to neuropsychiatric pathogenesis.

STAR★METHODS

RESOURCE AVAILABILITY

Lead contact—Further information and requests for resources should be directed to and will be fulfilled by the Lead Contact, Marc V. Fuccillo (fuccillo@pennmedicine.upenn.edu).

Materials availability—This study did not generate new unique reagents.

Data and code availability—All datasets generated during and/or analyzed during the current study and all custom MATLAB or Igor scripts are available from the Lead Contact upon request.

EXPERIMENTAL MODEL AND SUBJECT DETAILS

All experiments were conducted in accordance with the National Institutes of Health Guidelines for the Use of Animals, and all procedures approved by the Institutional Animal Care and Use Committee of the University of Pennsylvania (Protocol: 805643). Animal health was monitored daily, and only healthy animals were used in experiments. Animals used in experiments had not previously been involved in other experiments or exposed to any drugs. Animals were kept on a 12:12 light-dark cycle and provided food and water *ad libitum*.

Animals—Constitutive Nrxn1α KO mice were obtained from the Südhof lab and were kept on a C57BL/6 background (Stanford University) (Geppert et al., 1998). To yield mice for breeding, founders were crossed onto C57BL/6 (Jackson Laboratory) generating Nrxn1α$^{+/-}$ animals. To identify direct pathway and putative indirect pathway neurons, Nrxn1a$^{+/-}$ animals were subsequently crossed onto the Drd1a-tdTomato BAC transgenic line. Breeders for experimental animals were male and female Nrxn1α$^{+/-}$ animals with one breeder also hemizygous for D1Tom^{+}. Offspring were weaned at P21 and separated by sex in cages of 2-5 animals of mixed genotypes. Adult male mice between the ages of 3-5 weeks were used for experiments.

METHOD DETAILS

Stereotaxic surgeries—Viral injections were performed on a stereotaxic frame (Kopf Instruments, Model 1900) under isoflurane anesthesia (3% for induction; 1%–2% during surgery). Sterile surgical technique was used, removing fur over the skull with a depilatory cream, and applying 70% isopropyl alcohol and betadine. Prior to creating an incision in the scalp to access the skull, a local anesthetic, lidocaine, was given subcutaneously. Small (0.5mm) holes were drilled and a pulled glass capillary needle was carefully lowered into the brain. Coordinates relative to bregma used for the regions of interest include dorsal prefrontal cortex (AP: +1.9mm, ML: +/− 0.3mm, DV: −1.4mm) and parafascicular nucleus of thalamus (AP: −2.2, ML: +/− 0.75, DV: −3.7). Bilateral injections of AAV-DJ-hSyn-ChiEF-2a-Venus (volume: 300nl) were infused 100nl/min using a microinfusion pump (Harvard Apparatus, #70-3007). The capillary glass was kept in the target region for 5 minutes after viral infusion was complete to prevent backflow, brought up 0.2mm, and after an additional 5 minutes was slowly brought up out of the brain. Mice were sutured with non-absorbable monomid nylon sutures (Stoelting), subcutaneously injected with carprofen for inflammation, and given 3 weeks (for dPFC) or 4-5 weeks (for PFas) to allow for recovery and viral expression. Prior to acute slice recording, target site injections are confirmed by examining viral expression in the anterior slices (for dPFC) and posterior slices (for PFas).

Electrophysiology—Mice were deeply anesthetized and perfused transcardially with ice-cold artificial cerebrospinal fluid (ACSF) (pH 7.3-7.4) containing (in mM): 124 NaCl, 2.5 KCl, 1.2 NaH_2PO_4, 24 $NaHCO_3$, 5 HEPES, 12.5 glucose, 1.3 $MgSO_4$, $7H_2O$, 2.5 $CaCl_2$. The brain was rapidly removed, and coronal sections (250 μm) unless otherwise indicated, were cut on a vibratome (VT1200s, Leica). Slices were incubated in a holding chamber for 12-15 minutes at 32-34°C in a NMDG-based recovery solution (pH 7.3-7.4, pH adjusted with HCl) (in mM): 92 NMDG, 2.5 KCl, 1.2 NaH_2PO_4, 30 $NaHCO_3$, 20 HEPES, 25

glucose, 5 sodium ascorbate, 2 thiourea, 3 sodium pyruvate, 10 $MgSO_4$, $7H_2O$, 0.5 $CaCl_2$. Osmolarity for the NMDG-based solution and ACSF was kept between 300-310 mOsm. Following incubation, slices were moved to a second holding chamber containing ACSF at room temperature (20-22°C) for at least 1 hr. prior to recording. For recording, slices are transferred to the recording chamber (Scientifica) fully submerged in oxygenated (95% O_2, 5% CO_2) ACSF at a perfusion rate of 1.4-1.6 mL/min, bath temperature of 29-30°C, and secured using a slice anchor (Warner Instruments). Drugs were prepared in a stock solution of water or DMSO and diluted to their final concentration in ACSF. The final concentration of DMSO was < 0.1%. Electrophysiology data were acquired using custom-built Recording Artist software version (Dr. Rick Gerkin), Igor Pro 6.37 (Wavemetrics). All recordings were sampled at 20kHz, filtered at 2.8kHz except for the *in vivo* modeled trains that were sampled at 10kHz.

Intracellular recording—Striatal SPNs were visualized using differential interference contrast (DIC) video microscopy on an upright microscope (Olympus, BX51). Somatic whole-cell recordings were performed using borosilicate glass (World Precision Instruments, TW150-3) that had a tip resistance of 3-5 MΩ, filled with cesium-based internal for voltage-clamp recordings (in mM): 115 $CsMeSO_3$, 20 CsCl, 10 HEPES, 0.6 EGTA, 2.5 MgCl, 10 Na-Phosphocreatine, 4 Na-ATP, 4 Na-GTP, 0.1 Spermine, 1 QX-314 (pH adjusted to 7.3-7.4 with CsOH) or potassium-based internal (in mM): 140 K-gluconate, 5 KCl, 0.2 EGTA, 2 $MgCl_2$, 10 HEPES, 4 Mg-ATP, 0.3 Na-GTP, 10 Na-Phosphocreatine (pH adjusted to 7.3-7.4 with KOH). Voltage-clamp recordings were done holding the cell at a membrane potential of −70mV (unless otherwise indicated) using a MultiClamp 700B patch-clamp amplifier (Molecular Devices). Input resistance and access resistance were noted subsequently following membrane break-in, and cells with R_A >25 MΩ or R_I > 300 MΩ were discarded from further analysis.

For optogenetics, full-field 470nm illumination from a collimated light-emitting diode (LED) illuminator (CoolLED, PE-300) through a 40x objective (Olympus, 0.8NA water immersion) with a pulse width of 1ms was used to stimulate ChiEF-expressing axon terminals. To rule out somatic opsin contamination, an elongated light pulse was given following the last cell recorded in the slice. Optical-evoked voltage-clamp recordings were performed in the presence of picrotoxin (100 μM), a $GABA_A$ antagonist. AMPAR/NMDAR ratios were determined by comparing peak amplitude of averaged AMPAR EPSCs at −70mV (15 traces), with an averaged amplitude taken 50ms after optical stimulation of EPSCs recorded at +40mV (15 traces). LED intensities ranged from 0.042-0.543 mW/mm^2 during the optical input output measurements.

All miniature synaptic currents were recorded in the presence of tetrodotoxin (1 −M). For excitatory currents we used the cesium-based internal described above, however, for inhibitory currents we used an internal with high chloride to maximize IPSC amplitude (in mM): 135 CsCl, 10 HEPES, 0.6 EGTA, 2.5 MgCl, 10 Na-Phosphocreatine, 4 Na-ATP, 0.3 Na-GTP, 0.1 spermine, 1 QX-314. Excitatory currents were pharmacologically isolated with picrotoxin (100 μM) added to the ACSF to block $GABA_A$ receptors. To isolate inhibitory currents, D-APV (50 μM) and NBQX (10 αM) were added to block NMDARs and AMPARs, respectively.

Endocannabinoid-mediated depression—For the following experiments probing endocannabinoid signaling in Nrxn1α KO animals, recording pipettes were filled with a cesium-based internal solution (see above for recipe) and picrotoxin (100 μM) was bath-applied throughout the recording. SPNs were voltage-clamped at −70mV apart from DHPG where SPNs were held at −55mV throughout the recording. Paired-pulses with an inter-pulse interval of 50ms were delivered optically stimulating at 0.1Hz. Following a 10-minute stable baseline, drugs were bath-applied: DHPG (50 μM) was bath-applied for 10 minutes, followed by 20 minutes of recording in ACSF and in a separate experiment 1 μM URB 597 (Tocris, Cat# 4612) was bath-applied for 20 minutes. EPSC amplitudes were normalized to the average value during the initial baseline period. Paired-pulse ratios were calculated by the ratio of the averaged peak of the second EPSC to the averaged peak of the first EPSC.

Striatal field recordings and analysis—For the striatal field recordings, a pipette was filled with filtered ACSF and had an access resistance between 0.8-1.2 MΩ. Each recording was an average of ten trials unless otherwise indicated. These recordings produced a stereotyped waveform upon optogenetic stimulation consisting of two components. The fiber volley, the first component of the field recording, is measured using cursors in Igor Pro 7 whose minimum voltage is measured across a time window (around 0.5 ms to 3.5 ms after light stimulation). Slope measurements, used as an approximation of postsynaptic response, were performed by linear regression fit to the 10%-90% rising phase of the second component of the field.

Generation of spike train inputs—*In vivo* modeled inputs were generated by using *in vivo* single-unit recordings performed in dorsal striatum in mice during a behavioral task (provided by Dr. Alexxai Kravitz). Timestamps obtained from the single-unit recordings were approximately an hour in length. The recordings were binned by 500ms and two 30 s windows were taken from a single recording (total of five recording files used from 5 neurons recorded across 3 mice). The 30 s window was then thresholded for periods of inactivity defined as anything below 2Hz. The thresholded data was used as a “mask” to deliver more temporally representative durations of activity. The mask was populated with Poisson-distributed frequencies generated in MATLAB typical of dPFC regions - 5, 15, and 25Hz. In total, 10 unique optical patterns were generated. These patterns were randomized creating 5 templates. Therefore, each cell will see identical optical patterns, in addition to the order of the optical patterns being varied to remove pattern order as a potential confounding variable.

Tissue fixation and microscopy—Neurons were filled for 20-30 minutes via patch electrodes with 10 μM Alexa Fluor 488; hydrazide (Invitrogen). The tissue was immediately fixed with 4% paraformaldehyde in PBS buffer and left overnight at 4°C. The following day, slices were mounted in Vectashield (Vector Labs) and immediately imaged. Image acquisition of Alexa 488 fluorescence was performed on a Leica SP5II confocal microscope using a 40× oil immersion objective of NA 1.30, 2.50X zoom, and 488 nm laser. A z stack of each neuron was obtained with z-steps of 1 μm. Image analysis was performed using ImageJ (NIH) with a custom macro for spine counting. Images were analyzed “blindly” without

genotypic information available until spine quantification was completed. For each neuron, dendritic spines were counted from secondary branches of at least 50 μm in length.

Immunohistochemistry—Mice were perfused transcardially with 1 × PBS and 4% paraformaldehyde. Brains were post-fixed in 4% paraformaldehyde overnight. Brains were sectioned coronally at 50 μm on avibratome(Vibratome, Model 1000plus) in 1 × PBS solution. Free-floating sections containing striatum were blocked for 1 hr at 4° in blocking buffer containing 10% FBS, 1% BSA, and 0.2% Triton X-100 and subsequently incubated overnight with primary antibody: guinea pig anti-VGluT2 (EMD Millipore, Cat# AB2251-I) at 1:2500. The following day, sections were incubated for 2hr with secondary antibody: Alexa Fluor 647 goat anti-guinea pig (Jackson ImmunoResearch, Cat# 106-605-003) at 1:500.

QUANTIFICATION AND STATISTICAL ANALYSIS

Statistics—Statistics was performed with Graphpad Prism v7.0. All data are presented as the mean ± SEM, with N referring to the number of animals and n to the number of cells. See supplementary tables for statistical values and details of statistical tests. P values < 0.05 were considered significant.

Neuronal spiking was detected in NeuroMatic v.3.0 (Rothman and Silver, 2018) where further analysis was then performed in custom MATLAB (Mathworks) scripts. Miniature postsynaptic currents were measured in Minianalysis (Synaptosoft). Anatomical data examining spines were measured using script written for ImageJ (NIH) with investigator blinded to genotype. Z stacks were taken on a Leica SP5II confocal microscope (fluorescent). Image manipulation and figure generation were performed in ImageJ, Adobe Illustrator, and Adobe Photoshop.

Supplementary Material

Refer to Web version on PubMed Central for supplementary material.

ACKNOWLEDGMENTS

This work was supported by grants from the Howard Hughes Gilliam Fellowship and Behavioral and Cognitive Training Grant (T32-MH017168 to M.F.D.), NIMH (R01MH115030 to M.V.F.), and IDDRC Grant from the Children's Hospital of Philadelphia (to M.V.F.). We thank Nathan Henderson for his assistance with ImageJ, Alexandria Cowell for assistance with animal husbandry, Manivannan Subramaniyan for assistance in MATLAB coding, and Alexxai Kravitz for *in vivo* recording data that were used to design optical patterns. We also thank Kyuhyun Choi and members of the lab for insightful feedback on the manuscript draft and project.

REFERENCES

Ade KK, and Lovinger DM (2007). Anandamide regulates postnatal development of long-term synaptic plasticity in the rat dorsolateral striatum. J. Neurosci 27, 2403–2409. [PubMed: 17329438]

Ade KK, Wan Y, Chen M, Gloss B, and Calakos N (2011). An Improved BAC Transgenic Fluorescent Reporter Line for Sensitive and Specific Identification of Striatonigral Medium Spiny Neurons. Front. Syst. Neurosci 5, 32. [PubMed: 21713123]

Alabi O, Davatolhagh MF, Robinson M, Fortunato M, Cifuentes LV, Kable JW, and Fuccillo MV (2020). Disruption of Nrxn1α within excitatory forebrain circuits drives value-based dysfunction. eLife 9, e54838. [PubMed: 33274715]

Anderson GR, Aoto J, Tabuchi K, Földy C, Covy J, Yee AX, Wu D, Lee SJ, Chen L, Malenka RC, and Südhof TC (2015). β-Neurexins Control Neural Circuits by Regulating Synaptic Endocannabinoid Signaling. Cell 162, 593–606. [PubMed: 26213384]

Aoto J, Martinelli DC, Malenka RC, Tabuchi K, and Südhof TC (2013). Presynaptic neurexin-3 alternative splicing trans-synaptically controls post-synaptic AMPA receptor trafficking. Cell 154, 75–88. [PubMed: 23827676]

Asede D, Joseph A, and Bolton MM (2020). Deletion of Nrxn1α impairs long-range and local connectivity in amygdala fear circuit. Transl. Psychiatry 10, 242. [PubMed: 32684634]

Autism Genome Project Consortium; Szatmari P, Paterson AD, Zwaigenbaum L, Roberts W, Brian J, Liu XQ, Vincent JB, Skaug JL, Thompson AP, Senman L, et al. (2007). Mapping autism risk loci using genetic linkage and chromosomal rearrangements. Nat. Genet 39, 319–328. [PubMed: 17322880]

Balleine BW, Liljeholm M, and Ostlund SB (2009). The integrative function of the basal ganglia in instrumental conditioning. Behav. Brain Res 199, 43–52. [PubMed: 19027797]

Benthall KN, Ong SL, and Bateup HS (2018). Corticostriatal Transmission Is Selectively Enhanced in Striatonigral Neurons with Postnatal Loss of Tsc1. Cell Rep. 23, 3197–3208. [PubMed: 29898392]

Blundell J, Blaiss CA, Etherton MR, Espinosa F, Tabuchi K, Walz C, Bolliger MF, Südhof TC, and Powell CM (2010). Neuroligin-1 deletion results in impaired spatial memory and increased repetitive behavior. J. Neurosci 30, 2115–2129. [PubMed: 20147539]

Bucan M, Abrahams BS, Wang K, Glessner JT, Herman EI, Sonnenblick LI, Alvarez Retuerto AI, Imielinski M, Hadley D, Bradfield JP, et al. (2009). Genome-wide analyses of exonic copy number variants in a family-based study point to novel autism susceptibility genes. PLoS Genet. 5, e1000536. [PubMed: 19557195]

Budreck EC, Kwon OB, Jung JH, Baudouin S, Thommen A, Kim HS, Fukazawa Y, Harada H, Tabuchi K, Shigemoto R, et al. (2013). Neuroligin-1 controls synaptic abundance of NMDA-type glutamate receptors through extracellular coupling. Proc. Natl. Acad. Sci. USA 110, 725–730. [PubMed: 23269831]

Castronovo P, Baccarin M, Ricciardello A, Picinelli C, Tomaiuolo P, Cucinotta F, Frittoli M, Lintas C, Sacco R, and Persico AM (2020). Phenotypic spectrum of NRXN1 mono- and bi-allelic deficiency:A systematic review. Clin. Genet 97, 125–137. [PubMed: 30873608]

Cavaccini A, Gritti M, Giorgi A, Locarno A, Heck N, Migliarini S, Bertero A, Mereu M, Margiani G, Trusel M, et al. (2018). Serotonergic Signaling Controls Input-Specific Synaptic Plasticity at Striatal Circuits. Neuron 98, 801–816.e7. [PubMed: 29706583]

Chang J, Gilman SR, Chiang AH, Sanders SJ, and Vitkup D (2015). Genotype to phenotype relationships in autism spectrum disorders. Nat. Neurosci 18, 191–198. [PubMed: 25531569]

Chen M, Wan Y, Ade K, Ting J, Feng G, and Calakos N (2011). Sapap3 deletion anomalously activates short-term endocannabinoid-mediated synaptic plasticity. J. Neurosci 31, 9563–9573. [PubMed: 21715621]

Ching MSL, Shen Y, Tan W-H, Jeste SS, Morrow EM, Chen X, Mukaddes NM, Yoo S-Y, Hanson E, Hundley R, et al.; Children's Hospital Boston Genotype Phenotype Study Group (2010). Deletions of NRXN1 (neurexin-1) predispose to a wide spectrum of developmental disorders. Am. J. Med. Genet. B Neuropsychiatr. Genet 153B, 937–947. [PubMed: 20468056]

Choi S, and Lovinger DM (1997). Decreased probability of neurotransmitter release underlies striatal long-term depression and postnatal development of corticostriatal synapses. Proc. Natl. Acad. Sci. USA 94, 2665–2670. [PubMed: 9122253]

Choi K, Holly EN, Davatolhagh MF, Beier KT, and Fuccillo MV (2019). Integrated anatomical and physiological mapping of striatal afferent projections. Eur. J. Neurosci 49, 623–636. [PubMed: 29359830]

Chuhma N, Tanaka KF, Hen R, and Rayport S (2011). Functional connectome of the striatal medium spiny neuron. J. Neurosci 31, 1183–1192. [PubMed: 21273403]

Corbit VL, Manning EE, Gittis AH, and Ahmari SE (2019). Strengthened Inputs from Secondary Motor Cortex to Striatum in a Mouse Model of Compulsive Behavior. J. Neurosci 39, 2965–2975. [PubMed: 30737313]

Dabell MP, Rosenfeld JA, Bader P, Escobar LF, El-Khechen D, Vallee SE, Dinulos MB, Curry C, Fisher J, Tervo R, et al. (2013). Investigation of NRXN1 deletions: clinical and molecularcharacterization. Am. J. Med. Genet. A 161A, 717–731. [PubMed: 23495017]

Deng Y, Lanciego J, Kerkerian-Le-Goff L, Coulon P, Salin P, Kachidian P, Lei W, Del Mar N, and Reiner A (2015). Differential organization of cortical inputs to striatal projection neurons of the matrix compartment in rats. Front. Syst. Neurosci 9, 51. [PubMed: 25926776]

Ding J, Peterson JD, and Surmeier DJ (2008). Corticostriatal and thalamostriatal synapses have distinctive properties. J. Neurosci 28, 6483–6492. [PubMed: 18562619]

Doig NM, Moss J, and Bolam JP (2010). Cortical and thalamic innervation of direct and indirect pathway medium-sized spiny neurons in mouse striatum. J. Neurosci 30, 14610–14618. [PubMed: 21048118]

Doyle JP, Dougherty JD, Heiman M, Schmidt EF, Stevens TR, Ma G, Bupp S, Shrestha P, Shah RD, Doughty ML, et al. (2008). Application of a translational profiling approach for the comparative analysis of CNS cell types. Cell 135, 749–762. [PubMed: 19013282]

Ellender TJ, Harwood J, Kosillo P, Capogna M, and Bolam JP (2013). Heterogeneous properties of central lateral and parafascicular thalamic synapses in the striatum. J. Physiol 591, 257–272. [PubMed: 23109111]

Espinosa F, Xuan Z, Liu S, and Powell CM (2015). Neuroligin 1 modulates striatal glutamatergic neurotransmission in a pathway and NMDAR subunit-specific manner. Front. Synaptic Neurosci 7, 11. [PubMed: 26283958]

Etherton MR, Blaiss CA, Powell CM, and Südhof TC (2009). Mouse neurexin-1alpha deletion causes correlated electrophysiological and behavioral changes consistent with cognitive impairments. Proc. Natl. Acad. Sci. USA 106, 17998–18003. [PubMed: 19822762]

Földy C, Malenka RC, and Südhof TC (2013). Autism-associated neuroligin-3 mutations commonly disrupt tonic endocannabinoid signaling. Neuron 78, 498–509. [PubMed: 23583622]

Fuccillo MV (2016). Striatal Circuits as a Common Node for Autism Pathophysiology. Front. Neurosci 10, 27. [PubMed: 26903795]

Fuccillo MV, Földy C, Gökce Ö, Rothwell PE, Sun GL, Malenka RC, and Südhof TC (2015). Single-Cell mRNA Profiling Reveals Cell-Type-Specific Expression of Neurexin Isoforms. Neuron 87, 326–340. [PubMed: 26182417]

Geppert M, Khvotchev M, Krasnoperov V, Goda Y, Missler M, Hammer RE, Ichtchenko K, Petrenko AG, and Südhof TC (1998). Neurexin I alpha is a major alpha-latrotoxin receptor that cooperates in alpha-latrotoxin action. J. Biol. Chem 273, 1705–1710. [PubMed: 9430716]

Gerdeman GL, Ronesi J, and Lovinger DM (2002). Postsynaptic endocannabinoid release is critical to long-term depression in the striatum. Nat. Neurosci 5, 446–451. [PubMed: 11976704]

Gerfen CR (1989). The neostriatal mosaic: striatal patch-matrix organization is related to cortical lamination. Science 246, 385–388. [PubMed: 2799392]

Gerfen CR, Engber TM, Mahan LC, Susel Z, Chase TN, Monsma FJ Jr., and Sibley DR (1990). D1 and D2 dopamine receptor-regulated gene expression of striatonigral and striatopallidal neurons. Science 250,1429–1432. [PubMed: 2147780]

Giuffrida A, Parsons LH, Kerr TM, Rodríguez de Fonseca F, Navarro M, and Piomelli D (1999). Dopamine activation of endogenous cannabinoid signaling in dorsal striatum. Nat. Neurosci 2, 358–363. [PubMed: 10204543]

Graybiel AM, Aosaki T, Flaherty AW, and Kimura M (1994). The basal ganglia and adaptive motor control. Science 265, 1826–1831. [PubMed: 8091209]

Grayton HM, Missler M, Collier DA, and Fernandes C (2013). Altered social behaviours in neurexin 1α knockout mice resemble core symptoms in neurodevelopmental disorders. PLoS ONE 8, e67114. [PubMed: 23840597]

Heiman M, Schaefer A, Gong S, Peterson JD, Day M, Ramsey KE, Suárez-Fariñas M, Schwarz C, Stephan DA, Surmeier DJ, et al. (2008). A translational profiling approach for the molecular characterization of CNS cell types. Cell 135, 738–748. [PubMed: 19013281]

Huang CC, Lo SW, and Hsu KS (2001). Presynaptic mechanisms underlying cannabinoid inhibition of excitatory synaptic transmission in rat striatal neurons. J. Physiol 532, 731–748. [PubMed: 11313442]

Huang AY, Yu D, Davis LK, Sul JH, Tsetsos F, Ramensky V, Zelaya I, Ramos EM, Osiecki L, Chen JA, et al.; Tourette Syndrome Association International Consortium for Genetics(TSAICG);Gilles de la Tourette Syndrome GWAS Replication Initiative (GGRI) (2017). Rare Copy Number Variants in NRXN1 and CNTN6 Increase Risk for Tourette Syndrome. Neuron 94,1101–1111.e7. [PubMed: 28641109]

Hunnicutt BJ, Jongbloets BC, Birdsong WT, Gertz KJ, Zhong H, and Mao T (2016). A comprehensive excitatory input map of the striatum reveals novel functional organization. eLife 5, e19103. [PubMed: 27892854]

Kattenstroth G, Tantalaki E, Südhof TC, Gottmann K, and Missler M (2004). Postsynaptic N-methyl-D-aspartate receptor function requires alpha-neurexins. Proc. Natl. Acad. Sci. USA 101, 2607–2612. [PubMed: 14983056]

Kavalali ET (2015). The mechanisms and functions of spontaneous neurotransmitter release. Nat. Rev. Neurosci 16, 5–16. [PubMed: 25524119]

Kim HG, Kishikawa S, Higgins AW, Seong IS, Donovan DJ, Shen Y, Lally E, Weiss LA, Najm J, Kutsche K, et al. (2008). Disruption of Neurexin 1 Associated with Autism Spectrum Disorder. Am. J. Hum. Genet 82,199–207. [PubMed: 18179900]

Kirov G, Rujescu D, Ingason A, Collier DA, O'Donovan MC, and Owen MJ (2009). Neurexin 1 (NRXN1) deletions in schizophrenia. Schizophr. Bull 35, 851–854. [PubMed: 19675094]

Kreitzer AC, and Malenka RC (2005). Dopamine modulation of state-dependent endocannabinoid release and long-term depression in the striatum. J. Neurosci 25, 10537–10545. [PubMed: 16280591]

Kreitzer AC, and Malenka RC (2007). Endocannabinoid-mediated rescue of striatal LTD and motor deficits in Parkinson's disease models. Nature 445, 643–647. [PubMed: 17287809]

Kupferschmidt DA, Juczewski K, Cui G, Johnson KA, and Lovinger DM(2017). Parallel, but Dissociable, Processing in Discrete Corticostriatal Inputs Encodes Skill Learning. Neuron 96, 476–489.e5. [PubMed: 29024667]

Lenz JD, and Lobo MK (2013). Optogenetic insights into striatal function and behavior. Behav. Brain Res 255, 44–54. [PubMed: 23628212]

Lin JY, Lin MZ, Steinbach P, and Tsien RY (2009). Characterization of engineered channelrhodopsin variants with improved properties and kinetics. Biophys. J 96, 1803–1814. [PubMed: 19254539]

Lowther C, Speevak M, Armour CM, Goh ES, Graham GE, Li C, Zeesman S, Nowaczyk MJ, Schultz LA, Morra A, et al. (2017). Molecular characterization of NRXN1 deletions from 19,263 clinical microarray cases identifies exons important for neurodevelopmental disease expression. Genet. Med 19, 53–61. [PubMed: 27195815]

Maccarrone M, Rossi S, Bari M, De Chiara V, Fezza F, Musella A, Gasperi V, Prosperetti C, Bernardi G, Finazzi-Agrò A, et al. (2008). Anandamide inhibits metabolism and physiological actions of 2-arachidonoylglycerol in the striatum. Nat. Neurosci 11, 152–159. [PubMed: 18204441]

Mahon S, Vautrelle N, Pezard L, Slaght SJ, Deniau JM, Chouvet G, and Charpier S (2006). Distinct patterns of striatal medium spiny neuron activity during the natural sleep-wake cycle. J. Neurosci 26, 12587–12595. [PubMed: 17135420]

Mandelbaum G, Taranda J, Haynes TM, Hochbaum DR, Huang KW, Hyun M, Umadevi Venkataraju K, Straub C, Wang W, Robertson K, et al. (2019). Distinct Cortical-Thalamic-Striatal Circuits through the Parafas-cicular Nucleus. Neuron 102, 636–652.e7. [PubMed: 30905392]

Marshall CR, Howrigan DP, Merico D, Thiruvahindrapuram B, Wu W, Greer DS, Antaki D, Shetty A, Holmans PA, Pinto D, et al.; Psychosis Endophenotypes International Consortium; CNV and Schizophrenia Working Groups of the Psychiatric Genomics Consortium (2017). Contribution of copy number variants to schizophrenia from a genome-wide study of 41,321 subjects. Nat. Genet 49, 27–35. [PubMed: 27869829]

Miesenböck G (2011). Optogenetic control of cells and circuits. Annu. Rev. Cell Dev. Biol 27, 731–758. [PubMed: 21819234]

Missler M, Zhang W, Rohlmann A, Kattenstroth G, Hammer RE, Gottmann K, and Südhof TC (2003). Alpha-neurexins couple Ca2+ channels to synaptic vesicle exocytosis. Nature 423, 939–948. [PubMed: 12827191]

Packard MG, and Knowlton BJ (2002). Learning and memory functions of the Basal Ganglia. Annu. Rev. Neurosci 25, 563–593. [PubMed: 12052921]

Pak C, Danko T, Zhang Y, Aoto J, Anderson G, Maxeiner S, Yi F, Wernig M, and Südhof TC (2015). Human Neuropsychiatric Disease Modeling using Conditional Deletion Reveals Synaptic Transmission Defects Caused by Heterozygous Mutations in NRXN1. Cell Stem Cell 17, 316–328. [PubMed: 26279266]

Pan WX, Mao T, and Dudman JT (2010). Inputs to the dorsal striatum of the mouse reflect the parallel circuit architecture of the forebrain. Front. Neuroanat 4, 147. [PubMed: 21212837]

Reichelt AC, Rodgers RJ, and Clapcote SJ (2012). The role of neurexins in schizophrenia and autistic spectrum disorder. Neuropharmacology 62, 1519–1526. [PubMed: 21262241]

Rothman JS, Silver RA. 2018. NeuroMatic: An Integrated Open-Source Software Toolkit for Acquisition, Analysis and Simulation of Electrophysiological Data. Front Neuroinform. 2018 4 4;12:14. [PubMed: 29670519]

Rothwell PE, Fuccillo MV, Maxeiner S, Hayton SJ, Gokce O, Lim BK, Fowler SC, Malenka RC, and Südhof TC (2014). Autism-associated neuroligin-3 mutations commonly impair striatal circuits to boost repetitive behaviors. Cell 158, 198–212. [PubMed: 24995986]

Sara Y, Virmani T, Deák F, Liu X, and Kavalali ET (2005).An isolated pool of vesicles recycles at rest and drives spontaneous neurotransmission. Neuron 45, 563–573. [PubMed: 15721242]

Schizophrenia Working Group of the Psychiatric Genomics Consortium (2014). Biological insights from 108 schizophrenia-associated genetic loci. Nature 511, 421–427. [PubMed: 25056061]

Shen W, Flajolet M, Greengard P, and Surmeier DJ (2008). Dichotomous dopaminergic control of striatal synaptic plasticity. Science 321, 848–851. [PubMed: 18687967]

Sippy T, Lapray D, Crochet S, and Petersen CC (2015). Cell-Type-Specific Sensorimotor Processing in Striatal Projection Neurons during Goal-Directed Behavior. Neuron 88, 298–305. [PubMed: 26439527]

Skene NG, Bryois J, Bakken TE, Breen G, Crowley JJ, Gaspar HA, Giusti-Rodriguez P, Hodge RD, Miller JA, Murñoz-Manchado AB, et al.; Major Depressive Disorder Working Group of the Psychiatric Genomics Consortium (2018). Genetic identification of brain cell types underlying schizophrenia. Nat. Genet 50, 825–833. [PubMed: 29785013]

Smeal RM, Keefe KA, and Wilcox KS (2008). Differences in excitatory transmission between thalamic and cortical afferents to single spiny efferent neurons of rat dorsal striatum. Eur. J. Neurosci 28, 2041–2052. [PubMed: 19046385]

Stern EA, Kincaid AE, and Wilson CJ (1997). Spontaneous subthreshold membrane potential fluctuations and action potential variability of rat cortico-striatal and striatal neurons in vivo. J. Neurophysiol 77, 1697–1715. [PubMed: 9114230]

Stern EA, Jaeger D, and Wilson CJ (1998). Membrane potential synchrony of simultaneously recorded striatal spiny neurons in vivo. Nature 394, 475–478. [PubMed: 9697769]

Südhof TC (2008). Neuroligins and neurexins link synaptic function to cognitive disease. Nature 455, 903–911. [PubMed: 18923512]

Südhof TC (2018). Towards an Understanding of Synapse Formation. Neuron 100, 276–293. [PubMed: 30359597]

Tanimura A, Yamazaki M, Hashimotodani Y, Uchigashima M, Kawata S, Abe M, Kita Y, Hashimoto K, Shimizu T, Watanabe M, et al. (2010). The endocannabinoid 2-arachidonoylglycerol produced by diacylglycerol lipase alpha mediates retrograde suppression of synaptic transmission. Neuron 65, 320–327. [PubMed: 20159446]

Wall NR, De La Parra M, Callaway EM, and Kreitzer AC (2013). Differential innervation of direct- and indirect-pathway striatal projection neurons. Neuron 79, 347–360. [PubMed: 23810541]

Wang W, Li C, Chen Q, van der Goes MS, Hawrot J, Yao AY, Gao X, Lu C, Zang Y, Zhang Q, et al. (2017). Striatopallidal dysfunction underlies repetitive behavior in Shank3-deficient model of autism. J. Clin. Invest 127, 1978–1990. [PubMed: 28414301]

Willsey AJ, and State MW (2015). Autism spectrum disorders: from genes to neurobiology. Curr. Opin. Neurobiol 30, 92–99. [PubMed: 25464374]

Willsey AJ, Sanders SJ, Li M, Dong S, Tebbenkamp AT, Muhle RA, Reilly SK, Lin L, Fertuzinhos S, Miller JA, et al. (2013). Coexpression networks implicate human midfetal deep cortical projection neurons in the pathogenesis of autism. Cell 155, 997–1007. [PubMed: 24267886]

Wilson CJ, and Groves PM (1981). Spontaneous firing patterns of identified spiny neurons in the rat neostriatum. Brain Res. 220, 67–80. [PubMed: 6168334]

Wilson CJ, and Kawaguchi Y (1996). The origins of two-state spontaneous membrane potential fluctuations of neostriatal spiny neurons. J. Neurosci 16, 2397–2410. [PubMed: 8601819]

Wu YW, Kim JI, Tawfik VL, Lalchandani RR, Scherrer G, and Ding JB (2015). Input- and cell-type-specific endocannabinoid-dependent LTD in the striatum. Cell Rep. 10, 75–87. [PubMed: 25543142]

Wu X, Morishita WK, Riley AM, Hale WD, Südhof TC, and Malenka RC (2019). Neuroligin-1 Signaling Controls LTP and NMDA Receptors by Distinct Molecular Pathways. Neuron 102, 621–635.e3. [PubMed: 30871858]

Xiong Q, Znamenskiy P, and Zador AM (2015). Selective corticostriatal plasticity during acquisition of an auditory discrimination task. Nature 521, 348–351. [PubMed: 25731173]

Yin HH, and Knowlton BJ (2006). The role of the basal ganglia in habit formation. Nat. Rev. Neurosci 7, 464–476. [PubMed: 16715055]

Highlights

- Afferent input and target SPN-specific synaptic phenotypes in Nrxn1α mutant mice
- Reduced release probability underlies dPFC-iSPN changes in synaptic strength
- Loss of Nrxn1α alters postsynaptic NMDAR function at parafascicular-DMS synapses
- Decreased dPFC-iSPN synaptic efficacy seen across naturalistic input frequencies

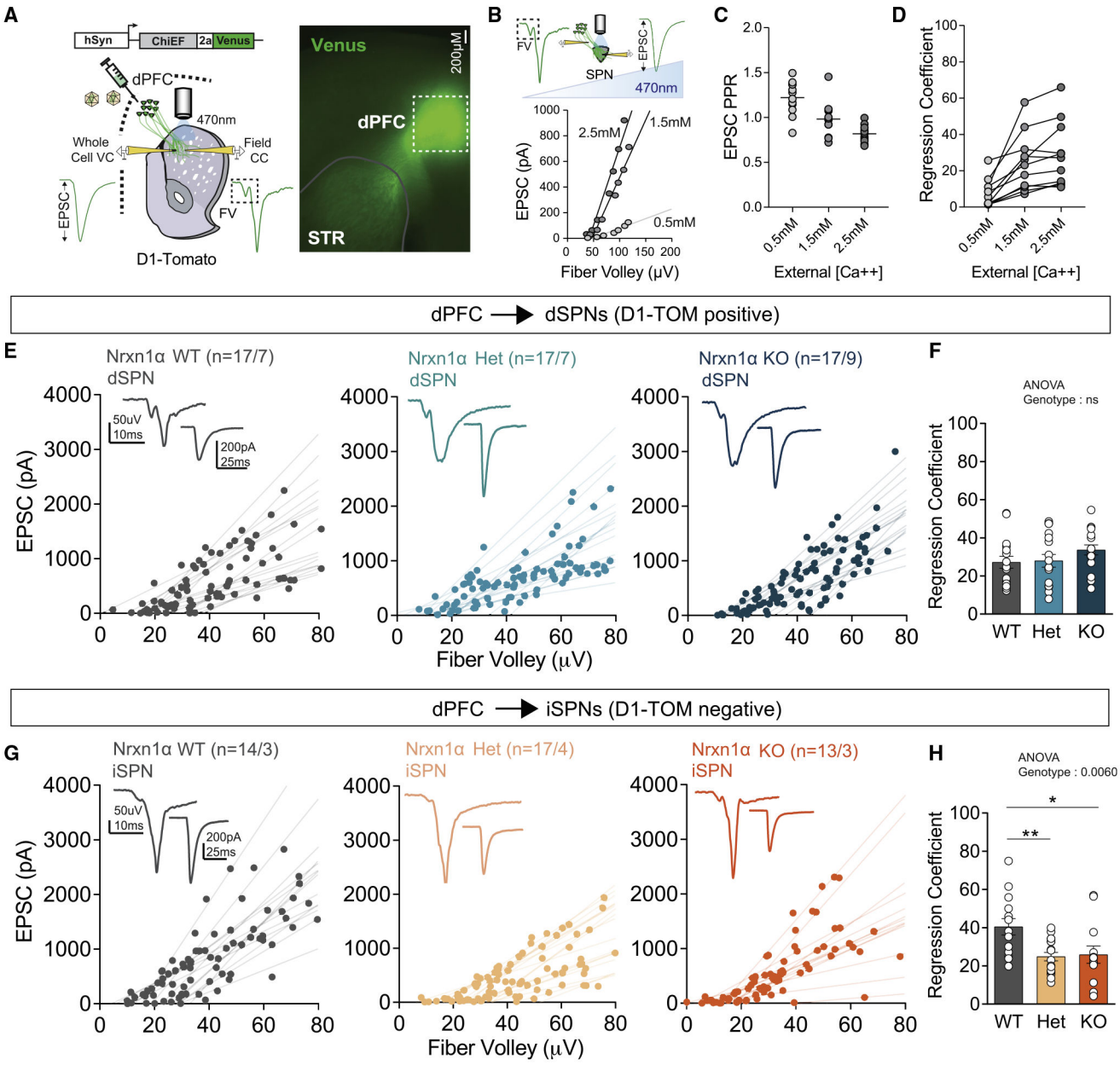

Figure 1. dPFC-DMS synapses exhibit a selective reduction in synaptic strength onto iSPNs in Nrxn1α Het and Nrxn1α KO animals

(A) Diagram of AAV constructs and combined whole-cell and field recording approach (left). Representative image (epifluorescence, 4× objective) showing ChiEF-2a-Venus expression in the dPFC (injection site, dotted white) and DMS (gray solid outline). Scale bar: 200 μM.

(B) Illustration of stepwise increase of 470-nm light-emitting diode (LED) intensity to measure a range of fiber volleys and postsynaptic EPSCs recorded in a combined whole-cell and field recording configuration (top). Representative cell depicting fitted lines from regression analyses of input/output measurements across varied external calcium levels.

(C) Paired-pulse ratio (50-ms ISI) is sensitive to external calcium levels (0.5, 1.5, 2.5 mM).

(D) Summary of regression coefficients from linear regression analyses performed on input/output measurements. Connected lines represent a neuron across varied external calcium levels.

(E and G) Plot of changes in fiber volley amplitude and EPSC across LED intensities in WT (left), Nrxn1α Het (middle), and Nrxn1α KO (right) of dSPNs(E) and iSPNs (G). Inset shows representative field recording with adjacent whole-cell recording below.

(F and H) Summary of regression coefficients of the linear regression analyses performed on the input/output measurements of dSPNs (F) and iSPNs (H). Each point represents a neuron. dSPN: WT, 17 cells/7 animals; Het, 17 cells/7 animals; KO, 17 cells/9 animals. iSPN: WT, 14 cells/3 animals; Het, 17 cells/4 animals; KO, 13 cells/3 animals.

Summary data are mean ± SEM; *$p < 0.05$, **$p < 0.01$. See also Figures S1-S4.

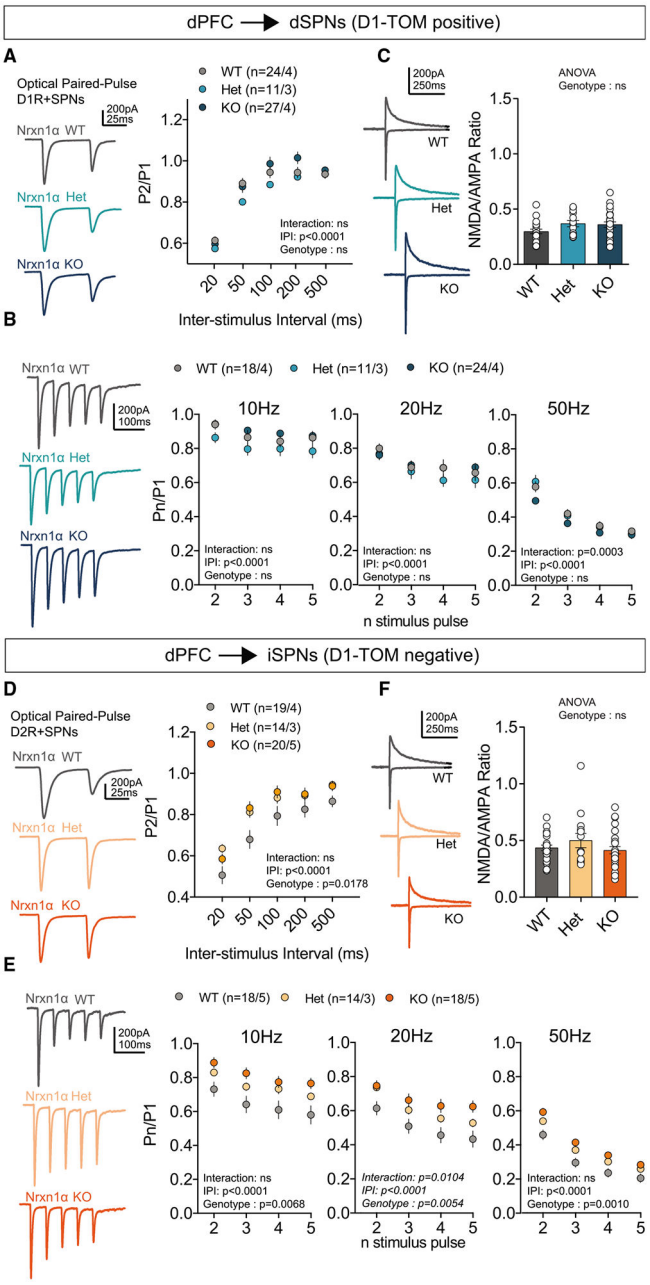

Figure 2. Reduced probability of release onto iSPNs at dPFC-DMS synapses in Nrxn1α Het and Nrxn1α KO animals

(A and D) Representative traces of paired-pulse response in each genotype (left; 50-ms ISI) and plot of paired-pulse ratio across multiple inter-stimulus intervals (ISI) (right) of dSPNs (A) and iSPNs (D). dSPN: WT, 24 cells/4 animals; Het, 11 cells/3 animals; KO, 27 cells/4 animals. iSPN: WT, 19 cells/4 animals; Het, 14 cells/3 animals; KO, 20 cells/5 animals. (B and E) Representative traces of five-pulse frequency trains (20 Hz; left) and plot of frequency trains across multiple frequencies (right; 10, 20, and 50 Hz from left to right) of dSPNs (B) and iSPNs (E). dSPN: WT, 18 cells/4 animals; Het, 11 cells/3 animals; KO, 24

cells/4 animals. iSPN: WT, 18 cells/5 animals; Het, 14 cells/3 animals; KO, 18 cells/5 animals.

(C and F) Representative traces of recordings used to measure NMDA/AMPA ratio (NMDA current is measured 50 ms from stimulation). Plot of NMDA/AMPA ratio by genotype (right) of dSPNs (C) and iSPNs (F). dSPN: WT, n = 21 cells; Het, n = 13 cells; KO, n = 26 cells. iSPN: WT, n = 22 cells; Het, n = 14 cells; KO, n = 26 cells. Summary data are mean ± SEM.

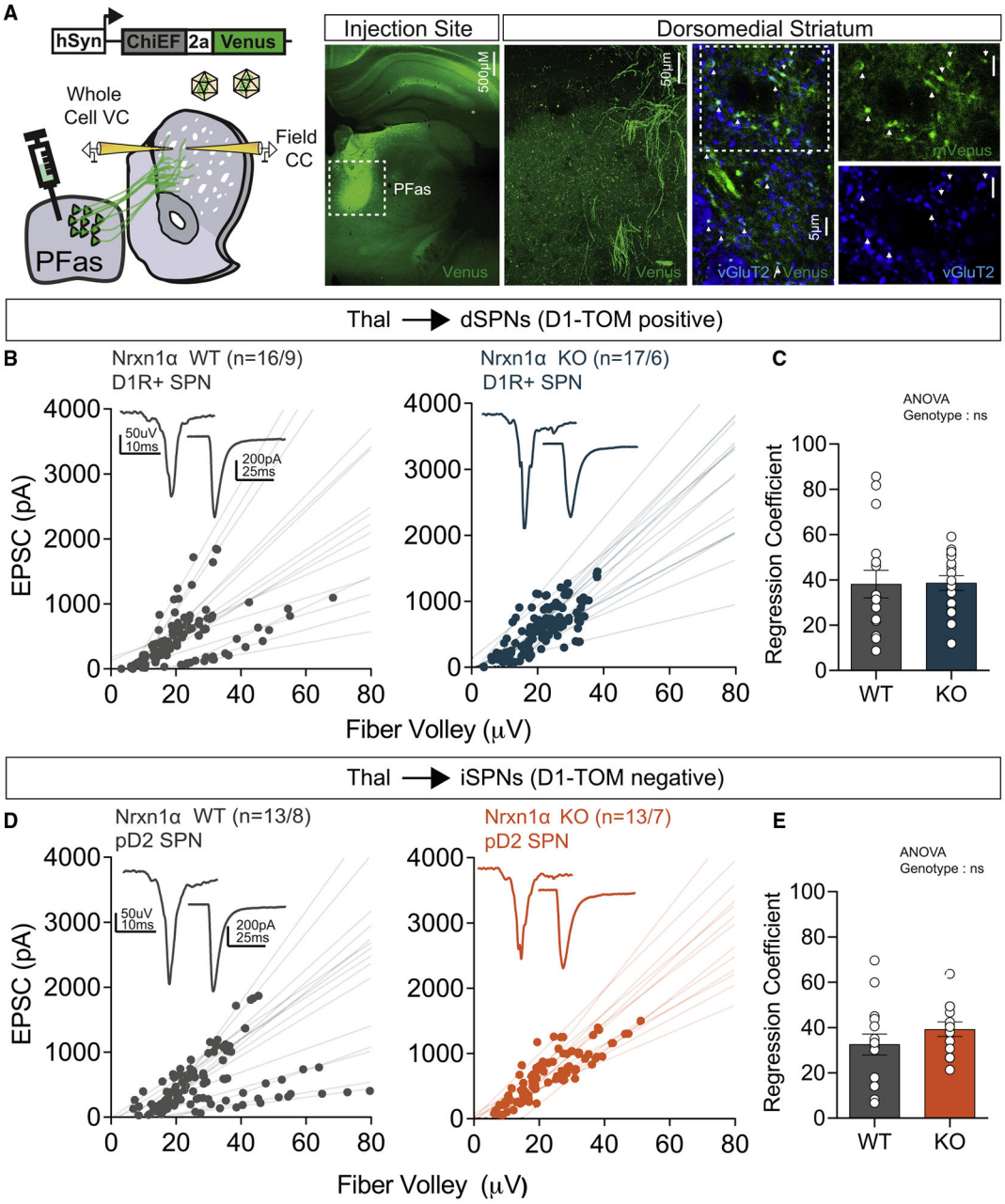

Figure 3. Synaptic strength is unaltered at PFas-DMS synapses in Nrxn1α KOs

(A) Experimental scheme of injection and recording sites for PFas-DMS projection (left). Representative image (epifluorescence, 4× objective, scale bar: 500 μM) of ChiEF-2a-Venus expression in PFas injection site (left) and opsin-expressing fibers (confocal, 20× objective, z stack max projection, scale bar: 50 μM). (Right) Immunohistochemistry staining for VGluT2 (blue) of striatal slices containing ChiEF-2a-Venus expression terminals originating from PFas. Arrows indicate co-localization. Scale bars: 5 μm for staining of VGluT2.

(B and D) Plot of changes in fiber volley amplitude and EPSC across LED intensities in WT (left) and Nrxn1α KO (right) of dSPNs (B) and iSPNs (D). Inset shows representative field recording with adjacent whole-cell recording below.

(C and E) Summary of regression coefficients of the linear regression analyses performed on the input/output measurements of dSPNs (C) and iSPNs (E). Each point represents a neuron. dSPN: WT, 16 cells/9 animals; KO, 17 cells/6 animals. iSPN: WT, 13 cells/8 animals; KO, 13 cells/7 animals.

Summary data are mean ± SEM.

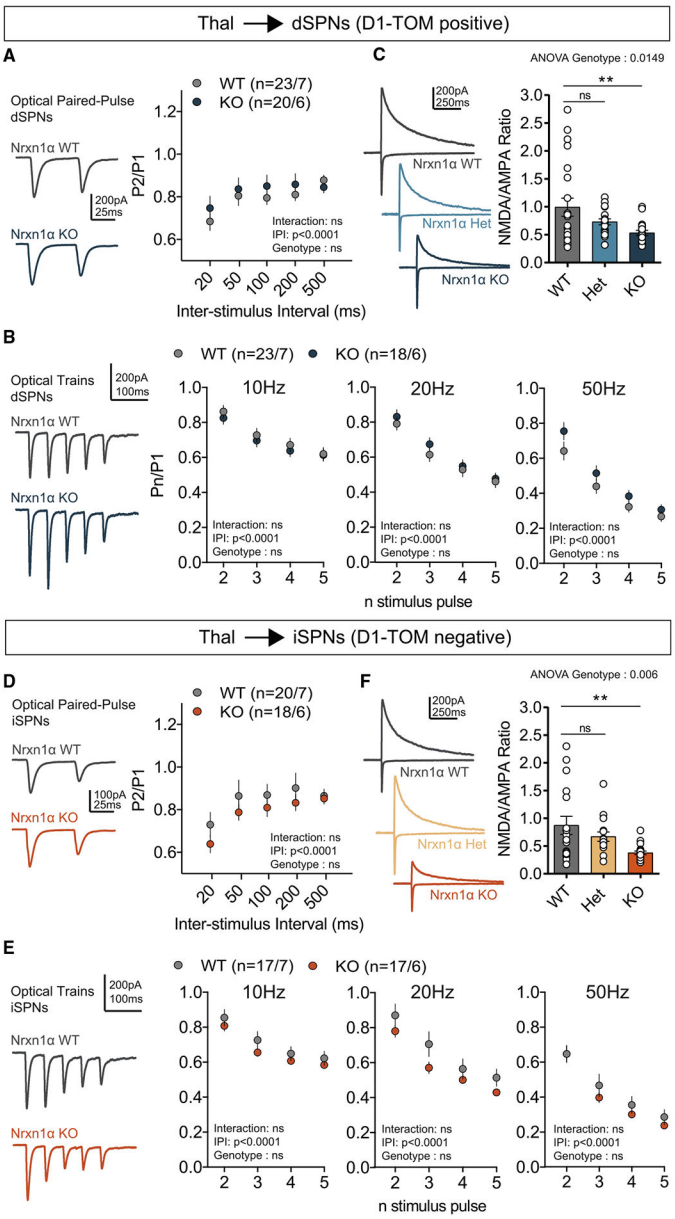

Figure 4. Altered postsynaptic function at PFas connections onto both SPN subtypes in Nrxn1α KO animals

(A and D) Representative traces of paired-pulse response in each genotype (left; 50-ms ISI) and plot of paired-pulse ratio across multiple ISIs (right) of dSPNs (A) and iSPNs (D). dSPN: WT, 23 cells/7 animals; KO, 20 cells/6 animals. iSPN: WT, 20 cells/7 animals; KO, 18 cells/6 animals.

(B and E) Representative traces of five-pulse frequency trains (20 Hz; left) and plot of frequency trains across multiple frequencies (right; 10,20, and 50 Hz from left to right) of dSPNs (B) and iSPNs (E). dSPN: WT, 23 cells/7 animals; KO, 18 cells/6 animals. iSPN: WT, 17 cells/7 animals; KO, 17 cells/6 animals.

(C and F) Representative traces of recordings used to measure NMDA/AMPA ratio (NMDA current is measured 50 ms from stimulation). Plot of NMDA/AMPA ratio by genotype

(right) of dSPNs (C) and iSPNs (F). dSPN: WT, n = 22 cells; KO, n = 19 cells. iSPN: WT, n = 17 cells; KO, n = 19 cells.

Summary data are mean ± SEM; *p < 0.05, **p < 0.01. See also Figure S5.

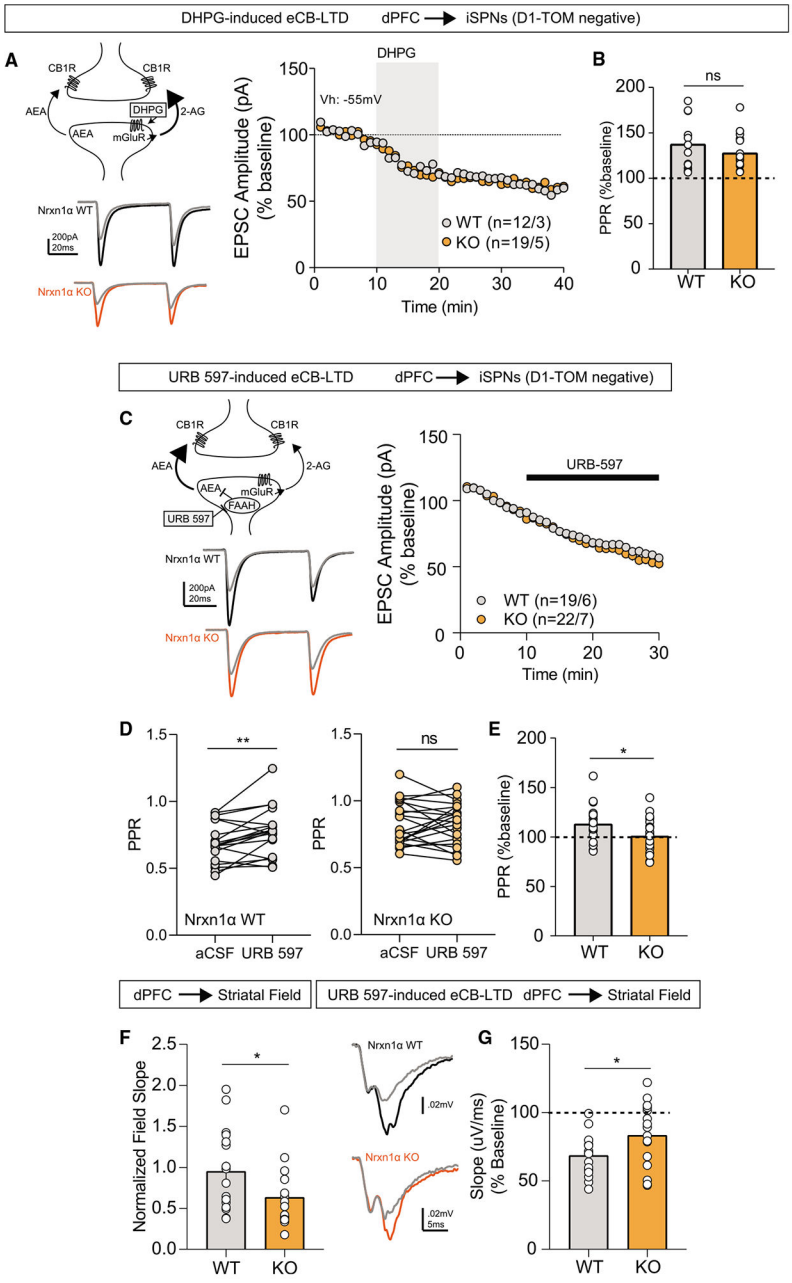

Figure 5. Endocannabinoid dysregulation through the anandamide pathway at dPFC-iSPN synapses of Nrxn1α KO mice

(A) Top left: schematic of the endocannabinoid signaling pathway stimulated by bath application of the group 1 mGluR agonist DHPG (50 μM) and depolarization (–55 mV). Activation of G_q-coupled mGluR results in the production of the endocannabinoid 2-arachidonoylglycerol (2-AG) and cannabinoid receptor activation. Bottom left: representative traces for Nrxn1α WT (black) and Nrxn1α KO (orange) at baseline, with overlaid traces (gray) for paired-pulse response in the presence of DHPG (50 μM), a mGluR1/5 agonist. Right: EPSC amplitude during baseline (10 min), bath application of DHPG (10 min), and 20 min in artificial cerebrospinal fluid (aCSF).

(B) Paired-pulse ratio (ISI: 50 ms), changes in PPR measured as the % change between baseline and the end of the recording to examine the changes in PPR in the presence of DHPG. WT, 12 cells/3 animals; KO, 19 cells/5 animals.
(C) Top left: schematic of the endocannabinoid signaling pathway stimulated by bath application of the fatty acid amide hydrolase (FAAH) inhibitor URB 597 (1 μM). FAAH regulates degradation of anandamide (AEA) and by selective inhibition of FAAH, AEA levels are elevated. Bottom left: representative traces for Nrxn1α WT (black) and Nrxn1α KO (orange) at baseline, with overlaid traces (gray) for paired-pulse response in the presence of URB 597 (1 μM), a FAAH inhibitor. Right: EPSC amplitude during baseline (10 min) and bath application of URB 597 (20 min).
(D) Paired-pulse ratio values (averaged 10 traces, ISI: 50 ms) before and after bath application of URB 597 for all neurons recorded in (left) Nrxn1α WT and (right) Nrxn1α KO.
(E) Paired-pulse ratio (ISI: 50 ms), changes in PPR measured as the % change between baseline and the end of the recording to examine the changes in PPR in the presence of URB 597. WT, 19 cells/6 animals; KO, 22 cells/7 animals.
(F) Optical striatal field responses between Nrxn1α WT and KO at baseline during aCSF. Slope of 10%–90% of the rising phase of the second component of the field is normalized to the fiber volley (first component of the field).
(G) (Left) Representative optical field recording traces for Nrxn1α WT (black) and Nrxn1α KO (orange) at baseline, with overlaid traces (gray) in the presence of URB 597. (Right) Changes between baseline and bath application of URB 597 of the slope of the field recording between genotypes.
Summary data are mean ± SEM; *$p < 0.05$, **$p < 0.01$.

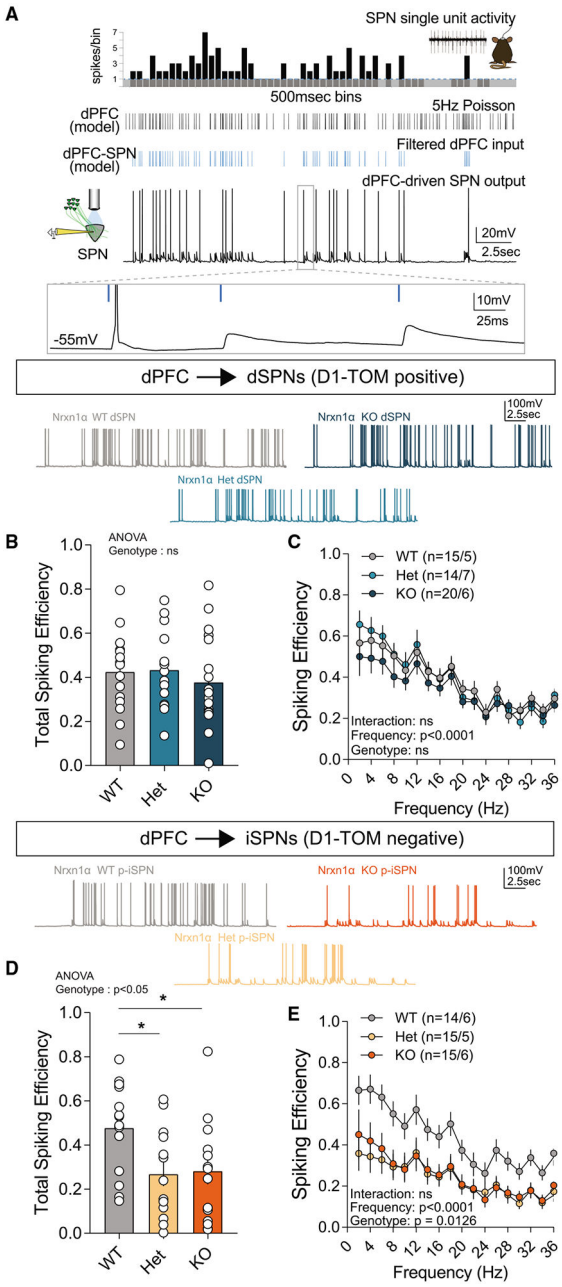

Figure 6. Reduced efficacy of dPFC-iSPN synapses across a broad range of naturalistic input frequencies in Nrxn1α KO mice

(A) Local inhibitory circuit remained intact for current-clamp recordings to permit a global view of synaptic efficacy. Optical stimulus patterns were modeled after SPN firing in *in vivo* single-unit recordings. (Top) Thresholded (>2 Hz, above dotted line) *in vivo* SPN activity is used as a mask for Poisson distributed cortical spike trains (black) to generate optogenetic pattern (blue). (Bottom) SPN spiking output to “modeled” dPFC-SPN inputs.

(B and D) Overall spiking efficiency for each dSPN and iSPN (D) recorded measured as the number of action potentials for a given optical pattern.

(C and E) Spiking efficiency across local frequencies represented in the filtered dPFC input stimulus for current-clamp recordings done in dSPNs and (E) iSPNs. dSPN: WT, 15 cells/5 animals; Het, 14 cells/7 animals; KO, 20 cells/6 animals. iSPN: WT, 14cells/6 animals; Het, 15 cells/5 animals; KO, 15 cells/6 animals. Spiking efficiency = action potentials/number of optical inputs.

Summary data are mean ± SEM; *$p < 0.05$. See also Figure S7.

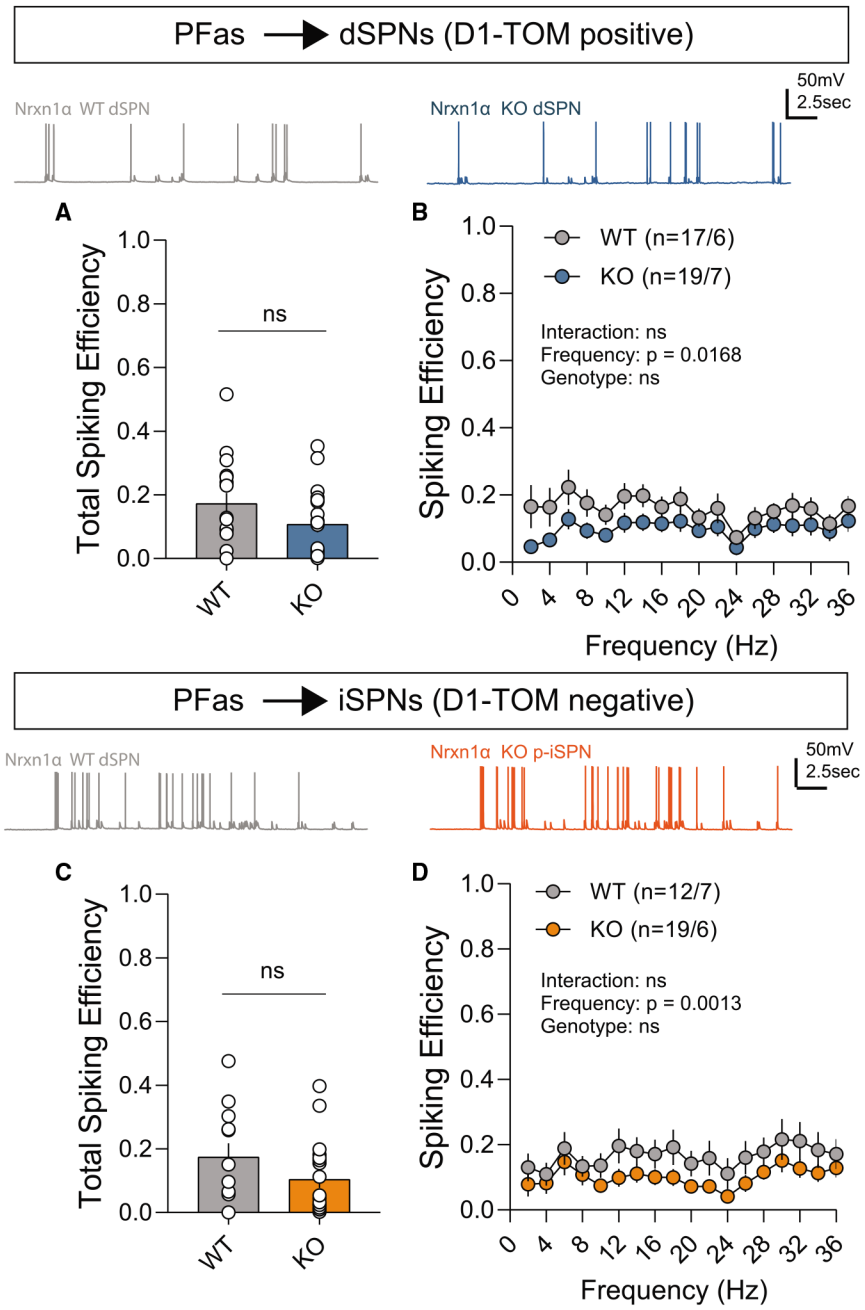

Figure 7. Synaptic efficacy unaltered at PFas projections onto both spiny projection neuron subtypes across a broad range of naturalistic input frequencies

(A and C) Overall spiking efficiency for each (A)dSPN and (C) iSPN recorded measured as the number of action potentials for a given optical pattern.

(B and D) Spiking efficiency across local frequencies for (B) dSPNs and (D) iSPNs. Identical frequencies were used as shown in Figure 6A. Representative traces shown for genotype and SPN subtype above graphs. dSPN: WT, 17 cells/6 animals; KO, 19 cells/7 animals. iSPN: WT, 12 cells/7 animals; KO, 19 cells/6 animals.

Summary data are mean ± SEM. See also Figure S7.

KEY RESOURCES TABLE

REAGENT or RESOURCE	SOURCE	IDENTIFIER
Antibodies		
Guinea pig anti-VGluT2	EMD Millipore	Cat. # AB2251-I; RRID: AB_2665454
Alexa Fluor 647 goat anti-guinea pig	Jackson ImmunoResearch	Cat. # 106-605-003; RRID: AB_2337446
Bacterial and virus strains		
pAAV-DJ-ChiEF-2a-Venus	Fuccillo lab	N/A
Chemicals, peptides, and recombinant proteins		
Tetrodotoxin (TTX)	Tocris	Cat. #1078
URB 597	Tocris	Cat. #4612
AM251	Tocris	Cat. #1117
Picrotoxin	Sigma Aldrich	Cat. #P1675
(S)-3,5-DHPG	Tocris	Cat. #0805
NBQX Disodium salt	Abcam	Cat. #ab120046
D-APV	Tocris	Cat. #0106
Vectashield	Vector Laboratories	Cat. # H-1400; RRID: AB_2336787
Alexa Fluor 488 Hydrazide	Invitrogen	Cat. #A10436
Experimental models: organisms/strains		
Nrxn1α Mouse (B6;129-*Nrxn1*^{tm1Sud}/J)	Südhof lab	N/A
Software and algorithms		
MATLAB	Mathworks	https://www.mathworks.com/products/matlab.html; RRID: SCR_001622
Igor Pro 6.37	Wavemetrics	https://www.wavemetrics.com/products/igorpro/igorpro.htm; RRID: SCR_000325
Recording Artist	Dr. Rick Gerkin	https://github.com/rgerkin/recording-artist
ImageJ	NIH	https://imagej.nih.gov/ij; RRID: SCR_003070
Minianalysis	Synaptosoft	http://www.synaptosoft.com/MiniAnalysis/; RRID: SCR_002184
NeuroMatic v. 3.0	Dr. Jason Rothman	http://www.neuromatic.thinkrandom.com/; RRID: SCR_004186
Graphpad Prism v7.0	Graphpad	https://www.graphpad.com/; RRID: SCR_002798